

Neutron Skin Measurement of Tin Isotopes



Dominika Glowka

Doctor of Philosophy
The University of Edinburgh
August 2015
June 2014

Abstract

Heavy atomic nuclei are thought to have proton and neutron radial distributions which have different extent. This difference is usually quantified in terms of a neutron skin (r_{np}), defined as the difference between the root mean square radii of the neutrons and protons radial distributions ($r_{np} = r_n^2 - r_p^2$). The nature or even existence of the neutron skin is currently not well established. Different nuclear theories give different predictions for the neutron skin thickness of a typical heavy nucleus ranging from 0.05 to 0.35 fm. Accurate measurement of the properties of the neutron skin would be a powerful constraint to differentiate between models of nuclear structure, improving our knowledge of the basic Equation Of State (EOS) for neutron rich matter. Particularly, the rate at which the neutron skin thickness changes across an isotopic chain of nuclei gives a tight constraint on the EOS and is also amenable to experimental determination with small systematic error. Improving our knowledge of the EOS for neutron rich matter is a crucial step to a deeper understanding of nuclear structure and nuclear matter in general. These results will also impact our knowledge of compact astrophysical objects such as neutron stars. This thesis describes the first measurement of neutron skin along an isotopic chain using an electromagnetic probe. The neutron skin is measured through the study of the coherent photoproduction of neutral pi mesons from nuclei.

This experiment was carried out in the A2 hall of the MAMI facility in Mainz, Germany in October 2012. The incident photon beam comprised energy tagged photons in the range of $E_\gamma=150\text{-}800$ MeV with an intensity of 10^8 sec^{-1} . Experimental data was obtained for three different tin targets, ^{116}Sn , ^{120}Sn and ^{124}Sn . The products from the resulting photoreactions were measured in the Crystal Ball detector and in the TAPS calorimeter systems, with track and particle identification information for charged particles provided by a multi wire

proportional chamber (MWPC) and a particle identification detector (PID).

The experiment provides the first information on the evolution of the neutron skin thickness along an isotopic chain using an electromagnetic probe. The results are compared with a range of theoretical models and previous data from strongly interacting probes. The new data will provide an important new experimental constraint on the basic properties of the EOS in atomic nuclei.

Chapter 1

Prologue

The composition of the world around us has been of unflagging interest to humanity throughout recorded history; the earliest known records attempting to explain the composition of matter date back to antiquity. Since 1911, when Rutherford elucidated the structure of the atom as being a compact dense nucleus surrounded by a more diffuse electron cloud, obtaining a better understanding of the nucleus has been a major endeavour of physics. Various experimental techniques have been developed to determine the size, shape and momentum distributions of atomic nuclei, providing a wealth of data from across the nuclear chart. As a result of precise experimental methods such as electron scattering and x-ray spectroscopy the charge distribution in nuclei has been estimated with high accuracy, for example the root mean square charge radius of ^{208}Pb is known to $\sim 0.01\%$ [18]. Despite a huge success of those experimental methods in determining the distribution of protons within a nucleus, the probes employed were largely insensitive to the neutron distribution in the nucleus. This was because the electrons dominantly interact with the charge in the nucleus and are only sensitive to uncharged components through the much weaker magnetic interaction. Strongly interacting probes such as protons, antiprotons and alpha particles do interact with neutrons, but their strong interactions and the resulting short mean free path of the probe in the nucleus have resulted in inconsistent determinations of the nature of the neutron distribution. The theoretical models describing these processes are subject to large model uncertainties due to uncertainties in the description of the strong interaction in the nuclear medium [73]. Currently it is not well established how

the distributions of neutrons differ from protons in the nucleus. Recent work using an electromagnetic probe and the method of coherent photoproduction of a neutral π meson has provided new constraints for ^{208}Pb (REF!!) with different systematics. This work will use this same technique to obtain the first assesment of how a neutron skin evolves across an isotopic chain of tin.

According to theoretical predictions of nuclear structure, nuclei with similar numbers of protons and neutrons have almost no difference between r.m.s. radii of charge and matter distributions. However, this situation is predicted to change with increasing mass number. It is predicted that for nuclei with the number of neutrons being much greater than the number of protons, the excess neutrons form a small skin around the nucleus. The size of this neutron skin is usually defined as:

$$\Delta R = r_n - r_p \tag{1.1}$$

where r_n and r_p are the r.m.s. radii of neutron and proton respectively [68]. Having ΔR determined accurately from experiment for a range of nuclei will provide a stringent constraint on current nuclear structure theories. There are many different theoretical models in common use, which predict very different values for the neutron skin; and experimental measurements could provide a means of verifying the validity of those models. Furthermore, an accurate measurement of the neutron skin will have far reaching implications in the field of nuclear physics. Currently, poorly established parameters in the equation of state for the neutron rich matter show a largely model independent linear dependence on the size of the neutron skin. Precise measurement of the neutron skin will put constraints on these parameters, which in turn will provide basis for understanding the physics of neutron stars, giving insights in properties such as the mass-radius relationship of low mass neutron stars and the feasibility of proposed cooling mechanisms such as modified URCA cooling.

Neutron skin measurements have been performed with strongly interacting probes before. The obtained data were strongly affected by many-body strong interaction effects that made the analysis and interpretation of the results ambiguous and made it difficult to draw a solid conclusion. The experiments involving proton scattering data, fitted with different neutron skin thicknesses, were inconclusive on the size or even the existence of the neutron skin [66].

The use of photons to study neutron skin potentially allows for much more accurate measurements than strongly interacting probes. The strength of photon's electromagnetic is weak if compared to the strong force. For these reasons the reaction is not as much affected by the initial state interactions (ISI) and the many-body interaction effects arising from multiple scatters of the incoming probe in the nucleus do not complicate the interpretation of the obtained data. Furthermore, because the electromagnetic interactions are better understood than strong interactions, the results obtained with the use of electromagnetic probes are less sensitive to systematic effects in their theoretical interpretation [73].

Coherent π^0 photoproduction takes place when a photon interacts with a target nucleon and as a result a π^0 meson is emitted, $A(\gamma, \pi^0)A$. Even though the photons are weakly interacting and unaffected by the ISI, the produced pions are strongly interacting particles and therefore the effect due to final state interactions (FSI) with the nucleus has to be accounted for. It has been shown previously that the strength of the FSI scales with pion energy and that the pion-nucleus scattering cross section is dominated by intermediate production of the $\Delta(1232)$ resonance on the struck nucleon. Pions with energies well away from the peak of the resonance have smaller probability of interaction with the nucleus. The study of coherent π^0 photoproduction provides therefore a unique way to not only test nuclear matter distribution, but to assess the theoretical treatment of pion-nucleus interactions as well.

The main objective of the experiment presented in this thesis is to exploit the coherent π^0 photoproduction as a means to study the nuclear matter distribution of three stable tin isotopes. In this way we were able to determine how the neutron skin thickness evolves increasing only the number of neutrons. The theoretical background to the experiment and methodology are presented in the next chapter. The experimental details are presented in the subsequent chapter. Then follows the summary of the current state of knowledge and a description of the implications of the results presented in this thesis for the future research. The next chapters present the analysis and experimental details while the results and conclusions are discussed in the final chapters.

Chapter 2

Theoretical Background

In 1932, Heisenberg formulated an idea that proton and neutron are in fact two states of the same particle, the nucleon. He proposed a new quantum number to label these states and he called it isospin (I) which in case of a nucleon carries a value of $\frac{1}{2}$. The Z components of the isospins for a proton and neutron, labelled as I_3 , are therefore $I_3 = \frac{1}{2}$ and $I_3 = -\frac{1}{2}$ respectively. Hence, the charge, Q , of the the nucleon can be written as:

$$\frac{Q}{e} = \frac{1}{2} + I_3 \quad (2.1)$$

where e is the charge of an electron.

In 1935, Yukawa, proposed that in order for the nucleons to be held together in a nucleus, some kind of "strong" force must exist and that the mediator particle for this force should be a spin-0 meson with a mass of $\sim 150MeV$ [21]. The existence of such particle has been proven 12 years later in 1947 when the charged pions were discovered by the collaboration of C. Powell, C. Lattes and G. Occhialini [54].

Pions are the lightest mesons with mass of $\sim 135MeV$ and they act as mediators of the long-range part of the strong nuclear force. They are zero spin particles composed of two valence quarks and they can be found in three states; neutral, (π^0), and charged, (π^+ and π^-).

Charged pions decay via weak interactions into muon and neutrino. The branching ratio of this decay mode is $\sim 99.9\%$ with a mean lifetime of $2.6 \times 10^{-8}s$.

$$\pi^+ \rightarrow \mu^+ + \nu_\mu \quad (2.2)$$

$$\pi^- \rightarrow \mu^- + \bar{\nu}_\mu \quad (2.3)$$

Other possible decay modes are into an electron and anti-neutrino, and a positron and neutrino. However, the probability of these decay channels is very low $\sim 0.001\%$.

Neutral pions decay via electromagnetic interactions with a mean lifetime of $8.4 \times 10^{-17}\text{s}$. The dominant decay mode (branching ratio of $\sim 99\%$) is into two photons:

$$\pi^0 \rightarrow \gamma + \gamma \quad (2.4)$$

The second most probable decay mode ($\sim 1\%$) is into a photon and an electron-positron pair [8].

2.1 Coherent pion photoproduction

Pion photoproduction occurs when a photon interacts with a nucleon and the reaction mechanism results in the emission of a pion in the final state. There are four possible channels of this reaction:

$$\gamma + p \rightarrow p + \pi^0 \quad (2.5)$$

$$\gamma + p \rightarrow n + \pi^+ \quad (2.6)$$

$$\gamma + n \rightarrow p + \pi^- \quad (2.7)$$

$$\gamma + n \rightarrow n + \pi^0 \quad (2.8)$$

Photoproduction can occur on a free nucleon (for example the proton nucleus of hydrogen) or for heavier elements from one of the nucleons bound within a nucleus. For heavier nuclei a coherent production process occurs only if the target nucleus is left in its ground state, $A_{gs}(\gamma, \pi^0)A_{gs}$. If the initial and final states differ, the process is incoherent. Because of the charge conservation, reactions involving charged pions leave the target nucleus in a different state than the original, therefore; the only coherent production possible is the one featuring neutral pions [73].

The π^0 production process occurs with a close to equal probability on both protons and neutrons for the photon energy ranges analysed in this experiment.

In the case of a coherent reaction there is not sufficient quantum information to identify which nucleon or shells of nucleons contributed to the reaction mechanism, therefore the amplitudes from all nucleons add coherently. The resulting production cross section, neglecting any final state interactions, is then directly proportional to the square of mass number, A , and the square of the matter form factor. In this Plane Wave Impulse Approximation (PWIA) the cross section is expressed as [27]:

$$\frac{d\sigma}{d\Omega} = A^2 \frac{q}{k_\gamma} P_3^2 |F_m(q)|^2 \sin^2(\theta_\pi) \quad (2.9)$$

where q is the momentum transferred to the nucleus, $F_m(q)$ is the matter form factor of the nucleus, P_3 is the contributing pion photoproduction amplitude [3]. The matter form factor is a Fourier transform of the matter density distribution and because of that a diffraction pattern can be observed in the differential cross section.

The use of photons to study neutron skin potentially allows for much more accurate measurements than strongly interacting probes. The strength of photon's electromagnetic interactions is very weak and as such they are not affected by the initial state interactions (ISI) and many-body interaction effects do not complicate the interpretation of the obtained data. Furthermore, the electromagnetic interactions are far better understood than strong interactions, and therefore, the results obtained with the use of electromagnetic probes are less susceptible to systematic effects in their theoretical interpretation [73].

Despite the photon probe in the entrance channel being close to ideal, the photoproduced pions are strongly interacting particles and therefore the effect of final state interactions (FSI) with the nucleus has to be accounted for. The real part of the pion-nucleus interaction is responsible for an angular shift in the (γ, π^0) angular distribution and the imaginary part, taking the absorption processes into account, explains the reduction in flux [3]. It has been shown previously that the strength of the FSI scales with pion energy and that the pion-nucleus scattering cross section is dominated by the $\Delta(1232)$ resonance corresponding to the pion energy of $\sim 165 MeV$. Photoproduced pions with energies away from the peak of the resonance have smaller interaction with the nucleus.

Although the FSI complicates the analysis of the matter distribution in the nucleus, they also provide a very effective way to study pion-nucleus interactions

across the whole volume of the nucleus. All the available information about those interactions comes from charged pions scattering experiments but due to very short lifetimes pions with energies lower than 30MeV could not have been used in those measurements. However, the coherent π^0 production is not constrained with the limitations of charged pions scattering experiments. It offers an opportunity to investigate the pion-nucleus interactions for pion energies nearing 0MeV evaluated over the entire volume of the nucleus [73].

The study of the coherent π^0 photoproduction provides therefore a unique way to test not only nuclear matter distribution but pion-nucleus interactions as well. The main objective of the experiment presented in this report is however, to use the coherent π^0 photoproduction as a mean to study the nuclear matter distribution of tin isotopes in order to determine how the neutron skin thickness depends on the mass number. The current predictions of neutron skin thicknesses of tin isotopes are presented in Fig. 2.1 below.

Across an isotopic chain from $A = 112$ to $A = 124$ we expect a change in the neutron skin of $\sim 0.05\text{fm}$ which should be easily detectable in the measurement.

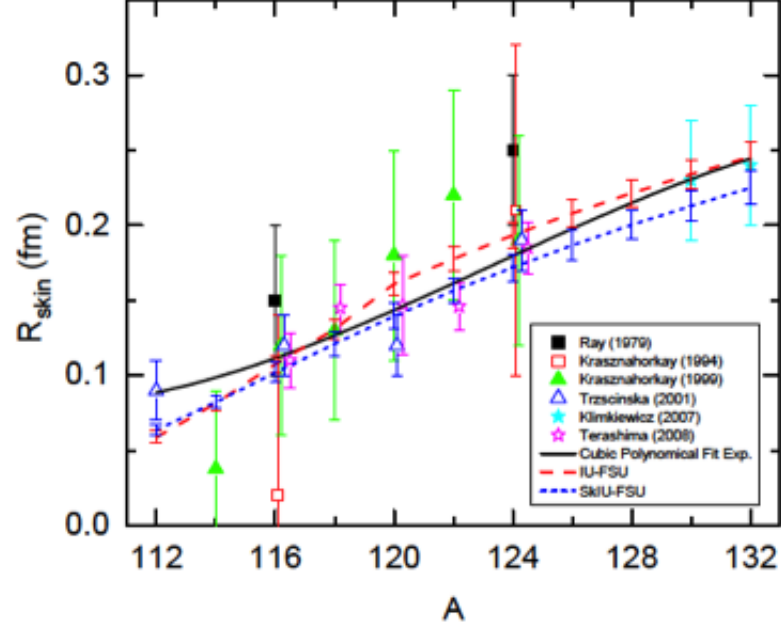


Figure 2.1: The predictions of the neutron skin thicknesses for tin isotopes from the IU-FSU and SkIU-FSU models after the optimization compared to those determined with other, different experimental methods [29].

2.1.1 Reaction kinematics

The schematics of the kinematics of a pion photoproduction reaction are shown in a figure below (Fig. 2.2). The interacting particles, photon (γ) and a nucleon (N) have initial four-momenta k and p_i respectively. The four-momentum is a combination of particle's energy and its three-momentum: $P=(p,E)$.

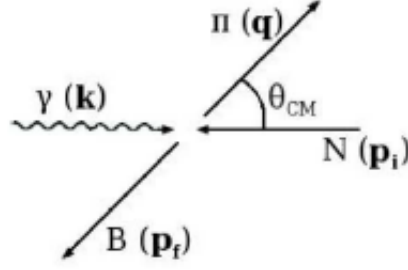


Figure 2.2: Simple diagram of a photoproduction reaction [55].

The Feynman diagrams shown below, illustrate that this reaction can proceed via three possible mechanisms (Fig. 2.3). First diagram, s-channel, describes a process where photon and nucleon combine into an intermediate particle (resonance) that eventually decays into two final state particles. In the case of t-channel, one of the interacting particles emits an intermediate particle which is subsequently absorbed by the other interacting particle. U-channel describes the same situation as t-channel with the exception of the final state particles being interchanged.

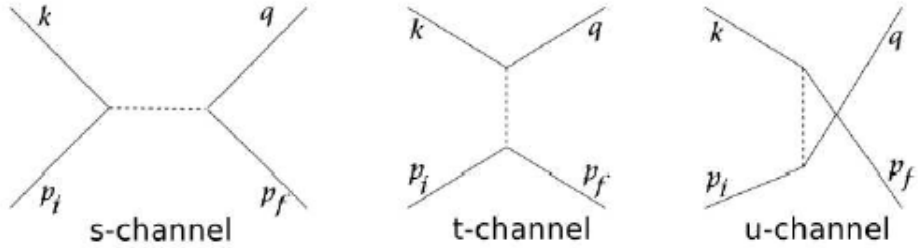


Figure 2.3: Feynman diagrams of the s-channel, t-channel and u-channel.

The kinematics of any such production reaction can be easily described with the use of Lorentz-invariant Mandelstam variables s , t and u . The mechanisms are commonly referred to as: s-channel, t-channel and u-channel (Fig. 2.3). They are defined in terms of four-momenta as [77]:

$$s = (k + p_i)^2 = (q + p_f)^2 \quad (2.10)$$

$$t = (p_i - p_f)^2 = (k - q)^2 \quad (2.11)$$

$$u = (p_i - p_f)^2 = (k - p_f)^2 \quad (2.12)$$

where, s is the square of the energy of the reaction, t is the square of the momentum transfer, while the sum of the squares of the masses of particles is defined as a linear combination of those three variables.

$$s + t + u = \sum m_i^2 \quad (2.13)$$

Only two of the Mandelstam variables are necessary to fully describe the reaction between photon and nucleon. In the relativistic approximation, $mc^2 \ll E$, these variables can be written as:

$$s = 4p^2 \quad (2.14)$$

$$t = 2p^2(1 - \cos\theta) \quad (2.15)$$

$$u = 2p^2(1 + \cos\theta) \quad (2.16)$$

where θ is the pion scattering angle in the center of mass frame of reference. If s is fixed, t is a linear function of $\cos\theta$, and therefore, the scattering functions can be represented completely in terms of s and $\cos\theta$ [12].

2.1.2 Reaction cross sections

For a pion, or any other meson, created in a photoproduction process, its angular distribution can be represented by a differential cross section:

$$\frac{d\sigma}{d\Omega} = |A(s, \cos\theta)|^2 \quad (2.17)$$

The probability of the transition from a given initial state $\langle i|$ to another final state $|f\rangle$ can be represented by a scattering matrix S in the Bjorken Drell notation [13]:

$$S_{fi} = \delta_{fi} - \frac{i}{(2\pi)^2} \delta^4(q - k + p_f - p_i) \sqrt{\frac{m_N^2}{4E_\gamma E_\pi E_i E_f}} \langle i|T|f \rangle \quad (2.18)$$

where, T is the transmission matrix relating initial and final states, m_N is the

mass of a nucleon, and q, k, p_i, p_f are four-momenta of the involved particles. The transmission matrix T describes the amplitude of the photoproduction process, and can be written as:

$$T = \epsilon_\mu J_\mu \quad (2.19)$$

where, ϵ_μ is the photon polarization vector and J_μ is the electromagnetic current of a nucleon. Then the differential cross section can be defined as:

$$\frac{d\sigma}{d\Omega} = \frac{q}{k} \left(\frac{m_N}{4\pi W} \right)^2 \sum |T| \quad (2.20)$$

where, W is the invariant mass of the system.

The electromagnetic current of a nucleon, J , as proposed by Chew, Goldberg, Low, Nambu (CGLN), can be written in terms of nucleon spin matrices, σ , and meson unit vectors \hat{q} and \hat{k} [46]:

$$J = \frac{q}{k} \frac{4\pi W}{m_n} (i\sigma F_1 + (\sigma \cdot \hat{k})(\sigma \times \hat{q})F_2 + i\bar{k}(\bar{\sigma} \cdot \hat{q})F_3 + i\bar{k}(\sigma \cdot \hat{k})F_4) \quad (2.21)$$

where,

$$\bar{\sigma} = \sigma - (\sigma \cdot \hat{q})\hat{q} \quad (2.22)$$

$$\bar{k} = \hat{k} - (\hat{k} \cdot \hat{q})\hat{q} \quad (2.23)$$

and F_1, F_2, F_3, F_4 , known as CGLN amplitudes, are the structure functions of energy and scattering angle, which can be written in terms of electric and magnetic multipoles and angular momentum through a partial wave expansion as:

$$F_1(\theta) = \sum_{l=0}^{\infty} (lM_{l+} + E_{l+})P'_{l-1}(\cos\theta) + ((l+1)M_{l-} - E_{l-})P'_{l-1}(\cos\theta) \quad (2.24)$$

$$F_2(\theta) = \sum_{l=0}^{\infty} ((l+1)M_{l+} + lM_{l-})P'_l(\cos\theta) \quad (2.25)$$

$$F_3(\theta) = \sum_{l=0}^{\infty} (E_{l+} - M_{l+})P''_{l+1}(\cos\theta) + (E_{l-} + M_{l-})P''_{l-1}(\cos\theta) \quad (2.26)$$

$$F_4(\theta) = \sum_{l=0}^{\infty} (M_{l+} - E_{l+} - M_l - E_{l-}) P''_l(\cos\theta) \quad (2.27)$$

where, P'_l and P''_l are derivatives of a Legendre polynomials, l is the relative orbital momentum of a meson, E_{\pm} and M_{\pm} are electric and magnetic transitions respectively, and the $+$ or $-$ determines whether the spin of the baryon should be added or subtracted.

The total angular momentum of a nucleon is $\frac{1}{2}$, and the total angular momentum of an incident photon is L_{γ} . In order to satisfy the selection rule, the resulting spin of a resonant state has to obey the following relation [10]:

$$\left| L_{\gamma} - \frac{1}{2} \right| < J_{N*} < \left| L_{\gamma} + \frac{1}{2} \right| \quad (2.28)$$

and the parity is given as:

$$\pi_{N*} = \pi_N \pi_{\gamma} \quad (2.29)$$

where, π_N , parity of a nucleon, is equal to 1, and π_{γ} , the parity of the photon is equal to:

$$\pi_{\gamma} = (-1)^{L_{\gamma}} \quad (2.30)$$

$$\pi_{\gamma} = (-1)^{L_{\gamma}+1} \quad (2.31)$$

respectively for an electric and magnetic multipoles.

The selection rules for the angular momentum and parity of the resonant state with respect to the outgoing meson are given as:

$$\left| L_{\pi} - \frac{1}{2} \right| < J_{N*} < \left| L_{\pi} + \frac{1}{2} \right| \quad (2.32)$$

$$\pi_{N*} = \pi_N \pi_{\pi} (-1)^{L_{\pi}} = (-1)^{L_{\pi}+1} \quad (2.33)$$

where π_{π} is -1.

Combining the above equations sets a limit on the spin and parity of the resonance:

$$\left| L_{\gamma} \pm \frac{1}{2} \right| < J_{N*} < \left| L_{\gamma} \pm \frac{1}{2} \right| \quad (2.34)$$

$$\pi_{N*} = \pi_{N\gamma} = (-1)^{L_\pi+1} \quad (2.35)$$

When a cross section is dominated by a single resonance, its quantum numbers are reflected in the angular distribution because of the dependence of the Legendre polynomials in the CGLN amplitudes. It means that the electric ($L = L_\pi \pm 1$) and the magnetic ($L = L_\pi$) multipoles, and the spin and parity are related to the angular distribution of mesons. Most photoproduction mechanism, however, have more than one multipole contributing to the resonance and in order to distinguish between the different contributions, several channels must be investigated.

Isospin, not conserved in the electromagnetic interactions, is conserved however, in the hadronic interactions. The isospin of the initial state, determined from the isospin of the nucleon, is $I_i = \frac{1}{2}$ while the contributions from the pion and nucleon's isospins determine the value of the isospin of the final state, I_f , which can therefore take values of $\frac{1}{2}$ or $-\frac{1}{2}$. The value is determined by the photon which behaves as a linear combination of an isoscalar (I_s), which conserves the isospin, and an isovector (I_v), which can change the isospin by one, components. The whole system can be then described by the three isospin amplitudes [60]:

$$A^0 = \langle \frac{1}{2}, I_3 | I_s | \frac{1}{2}, I_3 \rangle \quad (2.36)$$

for the isoscalar electromagnetic current, and:

$$A^1 = \langle \frac{1}{2}, I_3 | I_v | \frac{1}{2}, I_3 \rangle \quad (2.37)$$

$$A^3 = \langle \frac{3}{2}, I_3 | I_v | \frac{1}{2}, I_3 \rangle \quad (2.38)$$

for the isovector electromagnetic current.

As defined in [17], if the amplitudes are written as:

$$A^+ = \frac{A^1 + 2A^3}{3} \quad (2.39)$$

$$A^- = \frac{A^1 - A^3}{3} \quad (2.40)$$

the physical amplitudes for pion photoproduction can be expressed as:

$$A(p\gamma \rightarrow n\pi^0) = \langle p\pi^0 | I | p\gamma \rangle = (A^0 + A^+) \quad (2.41)$$

$$A(n\gamma \rightarrow n\pi^0) = \langle n\pi^0 | I | n\gamma \rangle = (A^+ + A^0) \quad (2.42)$$

$$A(p\gamma \rightarrow n\pi^+) = \langle n\pi^+ | I | p\gamma \rangle = \sqrt{2}(A^0 + A^-) \quad (2.43)$$

$$A(n\gamma \rightarrow p\pi^-) = \langle p\pi^- | I | n\gamma \rangle = \sqrt{2}(A^0 - A^-) \quad (2.44)$$

The above set of equations allows for the separation of the amplitudes for individual photoproduction reactions provided that the measurements on both proton and neutron targets are carried out.

2.1.3 Partial Wave Analyses

In order to extract information on the masses, widths and amplitudes from the experimental data, different reaction models have been developed and used. The most common approach involves separation of background and resonant terms of a transition matrix.

Considering a reaction of the form $A \rightarrow B \rightarrow C$, where A is the initial state of the nucleon-photon system, B is the intermediate resonant state and C is the final state of the nucleon-meson system, the photoproduction process can be described with a below Hamiltonian:

$$H = H_0 + V_{bg} + V_R(E) \quad (2.45)$$

where, H_0 is a free Hamiltonian expressing the total kinetic energy of the interacting particles, V_{bg} is the potential due to the background created by the non-resonant contributions to the reaction, and V_R is potential due to the resonant term.

The transition matrix for the process is given by:

$$T_{AC} = V_{AC} + \sum_B V_{AC} g_B(E) T_{BC}(E) \quad (2.46)$$

where, g_B is the propagator of the channel B of the reaction, and \sum_B sums all the possible channels of the reaction $A \rightarrow C$ via B . Alternatively, the transition matrix can be split into the background and resonant terms what allows the calculations for the background and resonant contributions to be carried out independently.

$$T^{AC} = t_{bg}^{AC} + t_R^{AC}(E) \quad (2.47)$$

Partial wave analyses (PWA) are methods that allow to decompose the background and resonant terms of the transmission matrix into a number of partial waves of defined multipoles and momentum. Generally, the resonant terms are modelled with a Breit-Wigner form while the background is described with Born terms and vector-meson contributions. The extraction of the parameters from the analysis is done in a two-stage procedure of fitting the experimental data. The most commonly used for the pion photoproduction PWAs are MAID, developed at the University of Mainz [2], and SAID written by the CNS Data Analysis Center at George Washington University [1].

MAID is a unitary isobar model which describes the transmission matrix through a single πN channel [20]:

$$T_{\gamma\pi} = V_{\gamma\pi}(E) + V_{\gamma\pi}(E)g_0T_{\pi N}(E) \quad (2.48)$$

where, $V_{\gamma\pi}$ is the transition potential of the $\gamma N \rightarrow \pi N$ reaction, $T_{\pi N}$ and g_0 are the scattering matrix and the free propagator of the πN interaction respectively.

The scattering matrix and the transition potential can be broken down to its constituents: background and resonant terms, which can be expanded as partial waves. The resonances included in MAID, classified as 4* by the Particle Data Group (PDG) [33], however, MAID can only fit the resonances up to $2GeV$.

In the methods developed for SAID, there are no assumptions about resonances and channels included in the analysis framework. The transmission matrix, defined for the following three channels: γN , πN and $\pi\Delta$ (covering all open channels), can be written as [41]:

$$T_{\gamma\pi} = A_1(1 + iT_{\pi N}) + A_RT_{\pi N, \pi N} \quad (2.49)$$

where A_R parametrizes the multipole amplitudes of the resonant terms, and A_1 parametrises background.

$$A_R = \frac{m_\pi}{q} \left[\frac{k}{q} \right]^l \sum_{n=0}^N p_n \left[\frac{E_\pi}{m_\pi} \right] \quad (2.50)$$

$$E_\pi = \frac{s - (m_\pi + M)^2}{2M} = E_\gamma - m_\pi \left(1 + \frac{m_\pi}{2M}\right) \quad (2.51)$$

where E_π is the pion kinetic energy in the lab frame for the $\pi N \rightarrow \gamma N$, s is the square of the center of mass energy, M is the mass of the nucleon. E_γ is the energy of the photon in the lab frame of reference for the $\gamma N \rightarrow \pi N$ reaction, and p_n is a free parameter determined in the fit to the experimental data.

$$A_1 = A_B + A_Q \quad (2.52)$$

where, A_B is a partial wave of a pseudoscalar Born amplitude, and A_Q is a Legendre function.

Detailed explanation of MAID and SAID can be found in [2, 20] and [1, 41].

2.2 Nuclear Matter Distribution

The charge distributions for many stable nuclei have been thoroughly investigated in the electron and proton elastic scattering [7, 11, 31]. And because of the very good understanding of the electromagnetic interaction, the charge radii are measured with a high degree of accuracy [18, 45]. The calculations of the matter radius from the proton scattering experiments, however, are much less accurate because the nucleon-nucleon interactions are not well understood.

Since an accurate measurement of the nuclear matter distribution and the determination of the neutron skin have been shown to have further implication for the studies of structure of the neutron stars, and understanding the isospin dependent bulk and surface properties of nuclear matter [49] many experiments investigating it have been carried out [43, 23, 32].

Those reasons alone would be a good motivation for a neutron skin measurement, however, using tin as the target offers additional research opportunities. Tin has many stable isotopes and its proton number is a magic number, making tin isotopes ideal for the studies of the systematic changes in neutron density distribution and the evolution of neutron skin along the isotopic chain. Furthermore, recent publications have shown that there exists a relation between the thickness of the neutron skin and the symmetry energy of the equation of state [14, 40, 36].

2.2.1 The nuclear Equation of State

From the definition, the equation of state (EOS) is a function of density (ρ) and isospin asymmetry (α) and it is expressed as the energy (E) per nucleon in the infinite nuclear matter, $\frac{E}{A}(\rho, \alpha)$ where α is expressed as:

$$\alpha = \frac{N - Z}{A} \quad (2.53)$$

where, N is the number of neutrons, Z is the number of protons and A is the atomic mass number.

The Bethe-Weizsaecker mass formula, more commonly known as semi-empirical mass formula (SEMF), based on the theory of the liquid drop model, have been first proposed in 1935 to explain the various properties of an atomic nucleus. According to the formula, the binding energy, E_B can be approximated as:

$$E_B = a_V A^3 - a_s A^{\frac{2}{3}} + a_C \frac{Z^2}{A^{\frac{1}{3}}} - a_A \frac{(A - 2Z)^2}{A} - \delta(A, Z) \quad (2.54)$$

where, a_V is the volume coefficient (based on the strong force), a_s , also based on the strong force, is the surface term which provides a correction to the volume term, a_C is the Coulomb or electrostatic term which introduces a correction due to electrostatic repulsion. a_A is the asymmetry coefficient, which is based on the Pauli exclusion principle, and accounts for the imbalances between numbers of proton and neutrons in a nucleus. The pairing term $\delta(A, Z)$ covers the effects of spin-coupling [12].

This formula, being one of the first and most widely used equation of states, gives a good description of the symmetric nuclear matter at nuclear densities. However, for the matter at higher densities and in the case of the assymetric matter, SEMF doesn't describe the experimental data well. Therefore, research into adapting the equation of state to such assymetric and high density matter is one of the most important studies in the fields of nuclear and particle physics.

An accurate measurements of the neutron skin could potentially put tighter constraints on the asymmetry term of the EOS and make it more aplicable in describing assymetric or high density matter encountered, for example, in the neutron stars.

2.3 Nuclear Theories

Ever since the formulation of the quantum mechanics, much of the research in the fields of nuclear and particle physics have been focused on the studies of the structure of the atomic nuclei. In those early times, the conventional theories treated nucleus as a quantum mechanical many-body problem of Fermions interacting through a non relativistic two-body potential defined by the Schroedinger equation [67]. In reality, this approach is not applicably for any but the lightest nuclei because the many-body problem cannot be resolved analytically. However, other methods developed and used in recent years, such as variational Monte Carlo and Green's function Monte Carlo techniques, have been successfully employed in solving non-relativistic many-body problems for nuclei with mass number greater than $10amu$ [16, 42]. For heavier nuclei those methods no longer hold and different approaches are required.

The Skyrme [28] or Gogny [34] interactions start off from the density dependent energy functions for iterative calculations of the Hartree-Fock. The parameters of these functions are then fitted to the experimental nucleon-nucleon scattering data.

The relativistic mean field (RMF) theory is a model of the nucleon-nucleon interactions assuming that nuclei are point-like particles described by Dirac spinors and all the interactions between them occur via mesonic fields. Even though there are many meson fields possible, most calculations only use the $\sigma(x)$, $\omega^\mu(x)$ and $\vec{\rho}^\mu(x)$ fields and the vector potential due to the photon exchange between the nucleons, $A^\mu(x)$ in order to simplify the calculations [57]. Just like Skyrme and Gogny forces, RMF theory also uses the Hartree-Fock variational methods to resolve the nuclear wavefunctions.

Most of the existing models used to describe the structure of nuclei are based either on the RMF theories or on the Skyrme or Gogny interactions. However, even though various models offer a fair degree of consistency when reproducing general properties of nuclear matter such as proton charge radius, they diverge when calculations of the neutron radius are considered [35, 25]. Fig. 2.4 shows discrepancies between neutron skin thickness calculations obtained from different models.

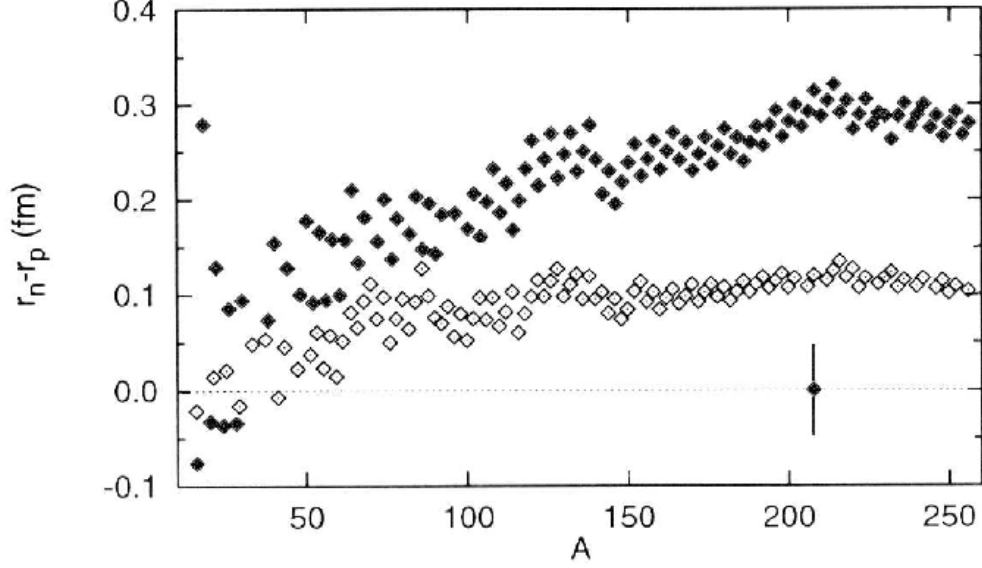


Figure 2.4: The variation of neutronskin thickness as predicted by different models. Filled markers are for the RMF theory calculations and empty markers show the predictions of the Skyrme forces. Taken from the reference [25].

2.4 Kamalov's DREN Calculations

The theoretical calculations done for this analysis were made using the code provided by S.Kamalov. The DREN (Delta Resonance Energy Model) calculations use the matter form factor (Fourier transform of the matter density distribution) as an input. The calculations are done under the assumption that both, matter and charge density distributions, $\rho(r)$, can be parametrised as a symmetries Fermi function:

$$\rho(r) = \rho_0 \frac{\sinh\left(\frac{c}{b}\right)}{\cosh\left(\frac{c}{b}\right) + \cosh\left(\frac{r}{b}\right)} \quad (2.55)$$

where, b is the diffuseness parameter, c is the half height radius and ρ_0 is defined as:

$$\rho_0 = \frac{3}{4\pi c^3} \left(1 + \frac{\pi b^2}{c}\right)^{-1} \quad (2.56)$$

Then the root mean square radius, r_{rms} , of the distribution is expressed as:

$$r_{rms} = \frac{3c^2}{5} \left(1 + \frac{7}{3} \left(\frac{\pi b}{c} \right)^2 \right) \quad (2.57)$$

The matter and charge distributions used in the calculations come from the recently provided by J. Piekarewicz RMF parameter set FSU-Gold [65]. The parameter set FSU-Gold introduces an isoscalar-isovector coupling term, Λ_v , which simulates the density dependence of the symmetry energy [71]. This parameter set has already been used and tested in the studies of the neutron skin of heavy nuclei [62], the equation of state for tin isotopes [63] and the investigation into different models of nuclear structure [64].

The calculations have been made for discrete values of photon energy in the E_γ range of $180 - 240 \text{ MeV}$ in 2 MeV steps. The results of those calculations for different targets are shown in the figure below:

Figure 2.5: The kamalov's DREN calculations of the cross sections for different targets, different E_γ and different FSU-Gold parameters sets.

2.5 Previous Measurements

Neutron skin measurements have been performed with strongly interacting probes before. The obtained data were strongly affected by many-body strong interaction effects that made the analysis and interpretation of the results ambiguous and difficult to draw binding conclusions from. The experiment involving proton scattering data fitted with different neutron skin thicknesses concluded with data being unable to determine the size or even the existence of the neutron skin [66].

The measurement of parity violation in electron scattering provides an independent probe of neutron densities because the weak charge of the neutron is much larger than that of proton. The interpretation of such results is model-independent and unaffected by the uncertainties of strong interactions. The polarized electrons have been used as a probe of neutron distribution in the ^{208}Pb Radius Experiment (PREX). It made use of parity violation to accurately determine the neutron radius of the lead nucleus. The first measurement of the

parity-violating asymmetry, A_{PV} in the elastic scattering of polarized electrons from ^{208}Pb reports the thickness of neutron skin of $\Delta R = 0.33^{+0.16}_{-0.18}\text{fm}$, and therefore provides the first electroweak observation of the neutron skin. [5].

The experiment investigating nuclear periphery at Low Energy Antiproton Ring (LEAR) at CERN allowed for an estimate of the relation between the symmetry parameter and neutron skin. 26 isotopes with mass numbers in a range of 40-238 have been studied. Antiprotons were chosen as a probe for the experiment since the antiproton-nucleus interactions are very strong and even a small overlap between their wave functions leads to the annihilation of the antiproton with one of the peripheral nucleons resulting in a final state nucleus with either proton or neutron number lower by one unit compared to the initial state. If both products are radioactive nuclear spectroscopy can be employed to determine their relative yields which are directly related to the proton and neutron densities at the annihilation site. The experimental results are presented in (Fig. 2.6); analysis of the data indicated that neutrons are distributed in a form of a halo rather than a skin [74]. However, as the antiprotons are absorbed only in the surface of the nucleus the systematics in such measurements are somewhat controversial.

Chapter 3

Experimental details

3.1 Overview

The experiment has been performed in the A2 hall of the MAMI facility at the Johannes Gutenberg Universitaet in Mainz, Germany in October 2012 over the course of 21 days.

The key element of the MAMI installation is the Mainzer Mikrotron; it provides a 100% duty factor electron beam that can be directed to any of the four experimental halls. The photon beam utilized in the experiment was produced by directing the electron beam onto a thin metallic radiator creating bremsstrahlung radiation. The Glasgow Photon Tagger analyses the recoiling electrons from the bremsstrahlung process and provides information on the energy of the photons. The tagger comprises of a large dipole magnet with an highly segmented detector apparatus near its focal plane. The tin target, located in the center of the Crystal Ball (CB), has been exposed to this bremsstrahlung photon. The products of the resulting photoreactions is then detected with the A2 segmented detectors. Since neutral pions have a very short lifetime, of the order of $\sim 10^{-18}s$ it is not possible to detect them directly. Instead, the products of their dominant decay, two photons, are detected in the apparatus and the pion's 4 momentum is reconstructed from this information. A schematic picture of the MAMI facility is presented In Fig. 3.1.

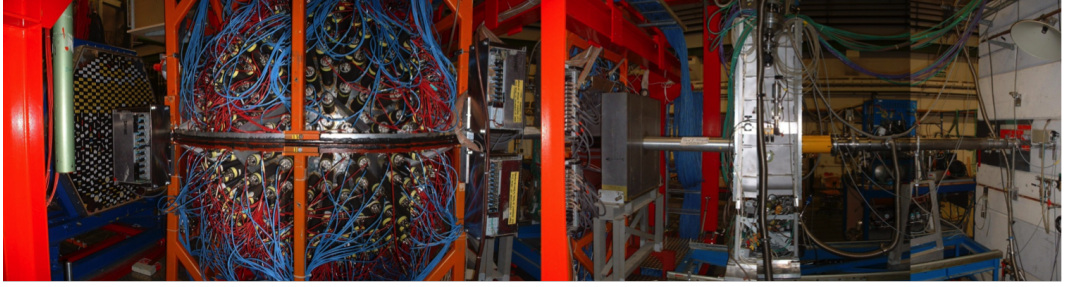


Figure 3.1: A diagram illustrating the experiential setup in the A2 hall at MAMI.

In addition to the CB and TAPS detectors we also used information from the Edinburgh Particle Identification Detector (PID), which provides information about charged particles detected in CB, and the Multi Wire Proportional Chambers (MWPC), which provides identification of charged particles and tracking information. The details of all the detectors as well as the MAMI facility itself are presented in the following sections.

3.2 Mainzer Mikrotron

The Mainz Microtron (MAMI) is a continuous wave electron accelerator. It is located at the Institut fuer Kernphysik at Johannes Gutenberg Universitaet in Mainz, Germany. MAMI operates since 1979 and in the interim period has been upgraded three times, achieving successively higher electron beam energies and intensities. The most recent upgrade, to MAMI-C, provides an electron beam energy up to 1.6GeV with an 80% helicity polarization and a beam current of over $20\mu A$ (unpolarized electron beams can reach up to $100\mu A$).

The MAMI facility operates using a racetrack microtron design. In this a beam of electrons is accelerated by a series of radio frequency LINAC (linear accelerator) sections and recirculated through the LINACs using a magnetic field. Each time the beam passes through the LINAC its orbit through the magnetic field changes, with higher energy electrons taking wider paths through the magnetic field. These paths are finely tuned such that the electrons always pass through the linac in time with the correct radiofrequency (rf) electric field applied to the LINACs. The design of the early stages of the MAMI RTM employs two homogeneous semicircular magnets and a small linear accelerator (LINAC) placed between

them (Fig. 3.2). Repeated passes through LINAC ensure that high beam energy can be achieved even if the acceleration with each pass is relatively small. The first microtron has been constructed at the National Research Council of Canada in 1947, according to the design of V. I. Veksler, where the electrons, accelerated along circular paths, reached energies of up to 4.6MeV [19]. Ever since that first design the idea of a microtron has been worked upon to reach higher electron energies. The concept of a racetrack microtron (RTM) has been proposed already in 1945 but the first RTM was constructed only in 1961 and provided electron beams of energies up to $\sim 12\text{MeV}$.

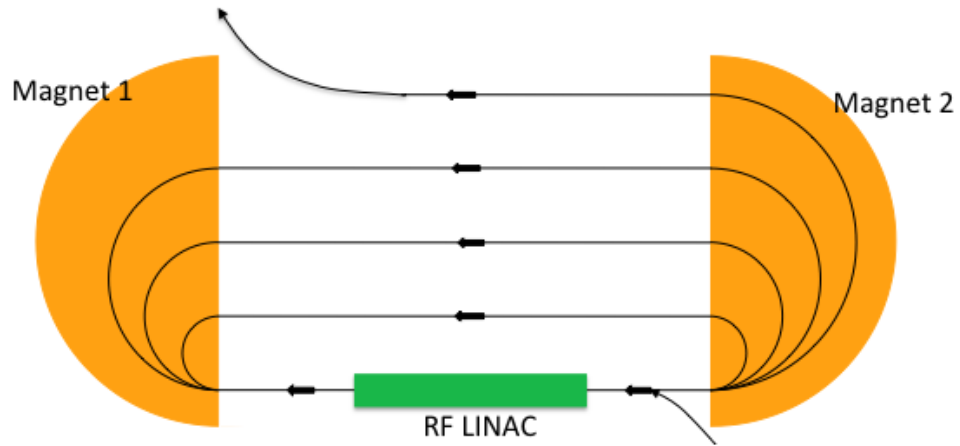


Figure 3.2: Schematics of a simple microtron.

In 1979 a RTM was first used successfully at the MAMI facility, producing an electron beam of 14MeV (MAMI-A1). Subsequent upgrade (MAMI-A2) introduced another RTM to the design and allowed for beam energies up to 180MeV in 1983. The need for even higher beam energies inspired yet another upgrade (MAMI B), and in 1990 with the addition of another RTM it was possible to achieve energies of up to 855MeV . However, quickly advancing research in the fields of nuclear and particle physics required even higher energies. The design allowing for beam energies of 1.5GeV however, could not employ another RTM based on the dipole magnet design; the magnets required for achieving such energies would have to weigh 2500 tons each which was neither financially nor spatially feasible; for comparison, magnets in the MAMI B design weigh only 450 tons. The issue has been bypassed by adding a harmonic double-sided microtron

(HDSM). In this concept, rather than using two magnets bending the beam by 180° , have been used four 90° magnets and two accelerating sections (Fig. 3.3).

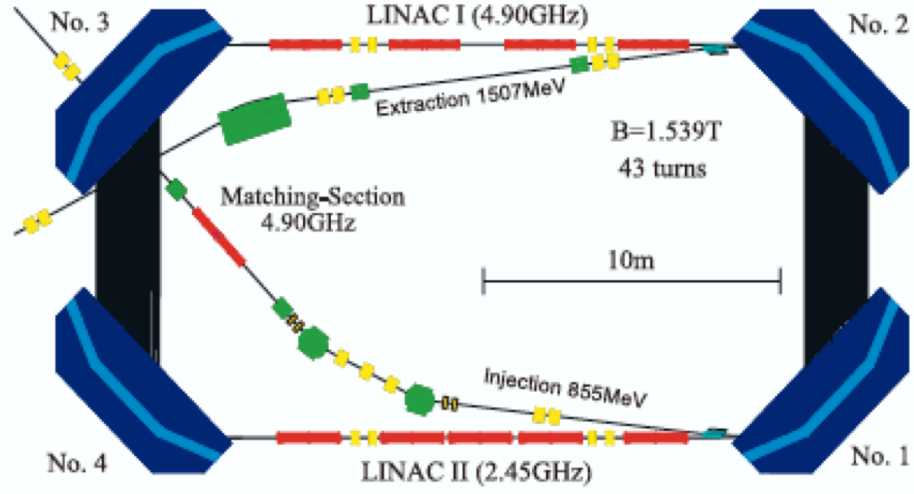


Figure 3.3: Schematic picture of a harmonic double-sided microtron for MAMI C.

This design allowed for the production of a 1.508GeV electron beam in December 2006, and energy as high as 1.604GeV has been reached in 2009.

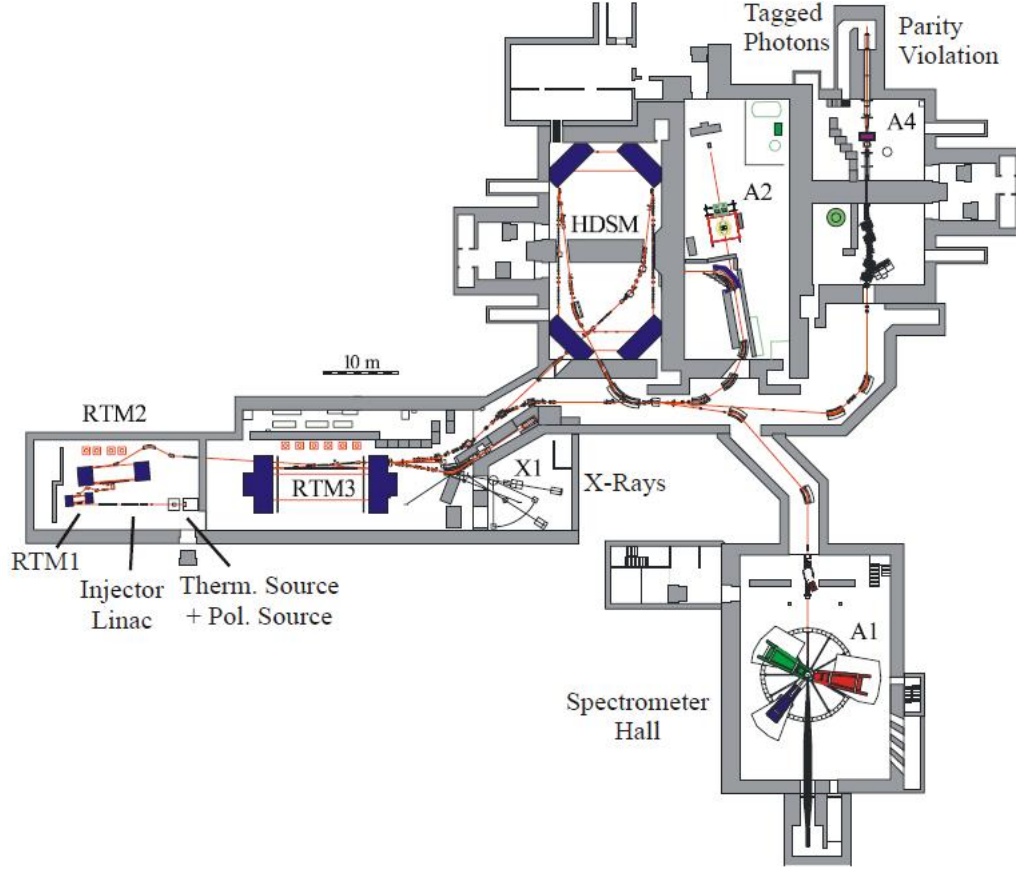


Figure 3.4: Floor plan of the MAMI facility.

3.3 Glasgow Photon Tagger

The experiment has been performed in the A2 hall of MAMI (Fig .3.4), which houses the installation dedicated to the studies of reactions between high-energy photons with different atomic nuclei. The photon beam used in this experiment has been produced through the electrons ejected from RTM3 which were directed into the A2 hall into a thin, $10\mu\text{m}$ thick, copper radiator. The 855MeV electrons can interact in the electrostatic field of the copper nuclei and radiate photons; the energy of these bremsstrahlung photons can be calculated from:

$$E_\gamma = E_0 - E_e \quad (3.1)$$

where E_0 is the initial beam energy and E_e is the energy of the scattered

electrons. This equation neglects the energy loss to the recoiling copper nuclei, however, the mass of the copper nucleus is high enough to assume that only negligible amount of kinetic energy has been transferred.

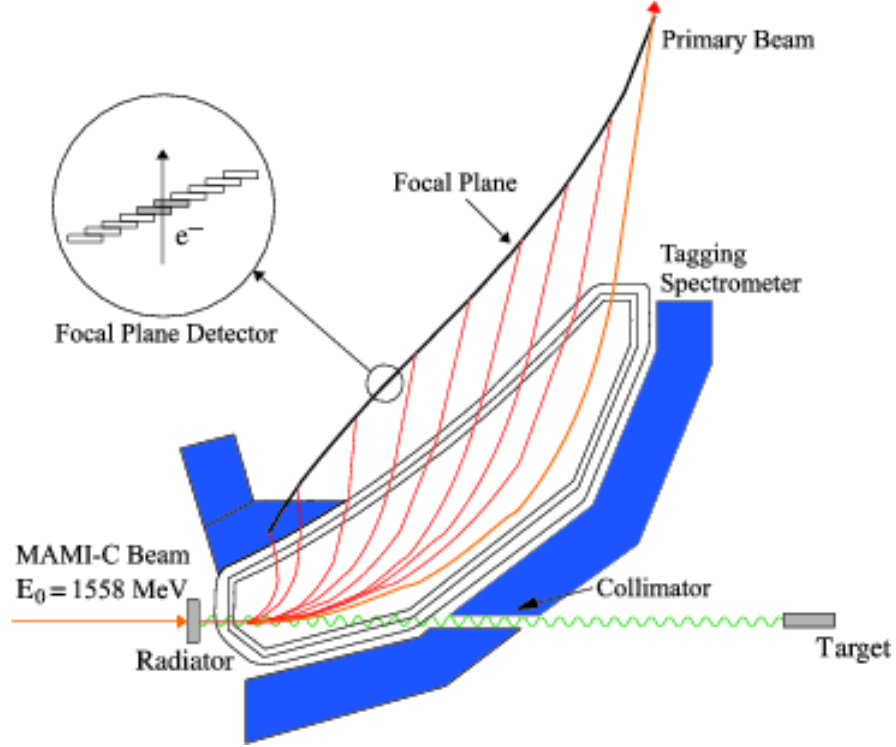


Figure 3.5: Schematic picture of the Glasgow Photon Tagger [76].

The Glasgow Photon Tagger (GPT) is a large momentum acceptance spectrometer. Electrons, after passing through the radiator, first enter the magnetic field of a quadrupole magnet, which focuses them vertically. After, the resulting electrons pass through a dipole magnet which disperses them horizontally according to their energy. For example, the lower energy electrons associated with the production of higher energy photons are bent more significantly by the field compared to the higher energy electrons. The momentum of the bremsstrahlung electrons is analyzed in the Glasgow Photon Tagger (Fig. 3.5). By identifying the path of the electron in the field and correlating the timing of the electron with the subsequent photonuclear reaction in the target then the photons can be characterized event-by-event. This is referred to as a tagged photon beam. Electrons that have radiated bremsstrahlung photons are directed

onto a segmented focal plane detector. The electrons that haven't radiated any photons follow a curved path into a beam dump.

The Focal Plane (FP) detector consists of 353 plastic scintillator detectors wrapped in a double-sided, aluminized Mylar [48]. Each of these scintillators is 80mm long and 2mm thick with a varying width of 9-32 mm. The detector width decreases along the focal plane in order to keep the energy resolution constant. The scintillators overlap by more than a half-width (Fig 3.2) which allows for electron detection by coincident signals in two adjacent detectors. The size of this overlap fixes the achievable energy resolution, which ranges from 2-8MeV with an average of 4MeV, depending on the beam energy [56]; the coincidence condition also allows for significant reduction of the low energy background in the detector.

Each scintillator is connected to an R1635 Hamamatsu photomultiplier tube (PMT), which are shielded from the magnetic field by 0.7mm thick steel plates and an individual sheath of μ -metal. The high segmentation of the array allows for the tagging of high-flux photon beams. When used with the 1.508GeV electron beam, the tagger can operate at a rate of up to 10^8 s^{-1} flux photons in the energy range of 0.08-1.401GeV. The maximum rate is determined by the operating limit of the individual PMTs being 1MHz per channel, limit used in order to avoid unnecessary reduction of their operating lifetime. The bremsstrahlung photons pass the magnetic field of the GPT unaffected and exit into the experimental hall through a channel bored into the dipole magnet.

In order to ensure the small size of the beam spot on the target a 3mm collimator is employed near to the exit of this bored channel. Employing a collimator produces a more well defined beam spot on the target, but also reduces the photon flux. Without collimation, the photon flux incident upon the target would be related more directly to the number of hits in the FP detector. To determine the exact luminosity of the photon beam, tagging efficiency measurements have to be made where a 100% efficient lead glass detector is placed in the beamline. This efficiency correction is applied individually to each detector channel in the focal-plane detector, as the efficiency depends on the opening angle of the gamma beam, which depends on the gamma (or electron) energy. The tagging efficiency is defined as:

$$\epsilon_{tagg} = \frac{N_\gamma}{N_e} \quad (3.2)$$

where N_γ is the number of photons passing through the collimator and registered by the lead glass detector, and N_e is the number of hits in the FP detector. During the tagging efficiency measurement, carried out as separate runs during the experiment, a lead glass detector is placed in the path of the collimated beam. The beam intensity employed in this measurement is lower than that used in the actual experiment in order to protect the lead glass detector from the potential radiation damage and to reduce the number of multiple hits in the FP detector.

3.4 Crystal Ball

The Crystal Ball (CB) has been constructed and used in various experiments long before being installed at MAMI. First used in the 1970s for colliding beam experiments at the SLAC facility to obtain first accurate measurements of $\frac{J}{\psi}$ [39]. Later it has been used at DESY and in Brookhaven National Laboratory and arrived in its current home, the A2 hall at MAMI only in 2002. The CB is an highly segmented calorimeter, it consists of 672 sodium iodide (NaI) crystals, each in a shape of truncated triangular pyramid, and arranged into a shape of a 20 sided polyhedron (Fig. 3.6).

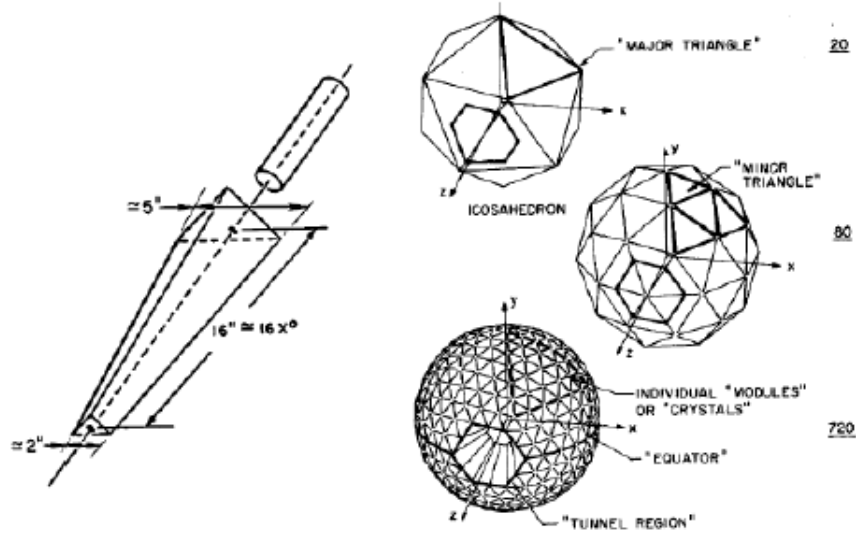


Figure 3.6: NaI crystal and CB geometry [4].

Having been designed for the colliding beam experiments, the plan had to accommodate the beamline running across and through the center of the CB. Because of that the section corresponding to 24 crystals on opposite poles of the sphere has been cleared making room for the beamline components. The remaining crystals have been grouped into two, hermetically sealed hemispheres; the isolation of the crystals from the outside environment was essential because NaI is an highly hygroscopic and it degenerates when exposed to the air moisture.

The outer and inner radii of the CB are 66cm and 25.3cm respectively. The two hemispheres are enclosed within a 1.5mm thick steel casing and the width of the gap between them, the equator region, is 0.8cm thick and consists of two 1.6mm thick steel plates and an adjustable air gap, usually set to 5mm. Such design allows for the coverage close to complete angular range, 94% of 4π .

The of the 20 faces (major triangle) of the CB polyhedron is segmented into 4 smaller triangles (minor triangle) which are in turn divided into 9 segments corresponding to individual NaI crystals (Fig. 3.6). Each crystal, 40.6cm long with the sides of the inner and outer faces being 5.1cm and 12.7cm respectively, is optically shielded with a reflector paper and aluminized Mylar, and connected to the 5.1cm diameter SRC L50 B01 PMT, chosen for a good linear response over

a wide range of energies. These are mounted outside the CB and scintillation light is fed into them through a 5cm air gap and a thick glass window, separating the NaI crystals from the PMTs. This set up constitutes part of the hermetic design helping to maintain isolated environment for the sodium iodide crystals. During the experiment photons produced in the reactions inside the CB trigger an electromagnetic shower which deposits energy in the NaI crystals. This system allows for good energy resolution across a wide range of energies. The amount of deposited energy and the number of crystals hit depend on the reaction studied; the information about the nature of the particles detected in the CB are recovered from the analysis of the hits in the NaI clusters; the basic detection properties of the CB are summarized in the below table [22].

Table 3.1: Crystal Ball Detection Parameters

Energy Photon Resolution		
	$\frac{\sigma}{E}$	$\sim \frac{1.7\%}{E(\text{GeV}^{0.4})}$
Angular Resolution		
	azimuthal:	$\sim \frac{2^\circ}{\sin\theta}$
	polar:	$\sim 2 - 3^\circ$
Angular Coverage		
	azimuthal:	0 - 360°
	polar:	20 - 160°
Time resolution		
		$\sigma \sim 2ns$

3.5 Multi Wire Proportional Chambers

Inside the tunnel region in the Crystal Ball another detector by the name of Multi Wire Proportional Chambers (MWPCs) is located. The task of this apparatus is to retrieve information about charged particles and it follows the same design as the one originally used in DAPHNE [24].

Each of the two MWPCs is built up of three layers; internal and external stripes acting as cathodes and a middle layer of wires as the anode (Fig. 3.7). The

cylindrical cathodes are made from 1mm thick rohacell laminated with aluminum stripes, 4mm wide and $0.1\mu\text{m}$ thick, spaced 0.5mm apart. The stripes are wound helically at 45° with respect to the anode wires, at opposite directions. The anode is made up of $20\mu\text{m}$ Tungsten wires 2mm apart placed parallel to the beam direction. The chambers are filled with a gas mixture of argon(79.5%), ethane (30%) and freon (0.5%).

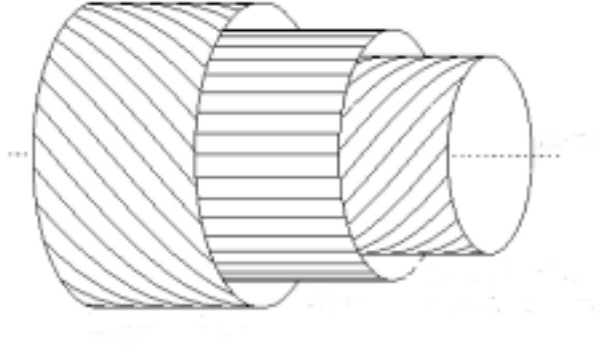


Figure 3.7: Diagram of MWPC showing the positions of anode wires and cathodes stripes [6].

Correlating the hits in both the cathode stripes and the anode wires will determine the tracks for charged particles. In the case of neutral particles experiments use the information provided by the MWPCs to determine the position of the target inside the CB. This information is extracted from the linear fit to the polar angle and z-position of the hits registered in both chambers to obtain the azimuthal and theta and angles for each track. Then the trajectories of multiple tracks are analyzed to find their intersection, and therefore obtain the position of the target. The design of the chambers allows this detector for full 360deg coverage of the azimuthal angle with polar coverage that ranges between 21° and 159° ; the characteristics of the MWPC chambers are summarized in the below table.

3.6 Particle Identification Detector

The Edinburgh Particle Identification Detector (PID) is located inside the Crystal Ball and it is surrounded by the MWPCs. It is a $\frac{dE}{dx}$ detector and, together with

Table 3.2: MWPC parameters

Angular Resolution	
azimuthal:	$\sim 1.8^{\text{deg}}$
polar:	2^{deg}
Angular Coverage	
azimuthal:	$0 - 360^{\circ}$
polar:	$21 - 159^{\circ}$

the CB apparatus, it provides information about charged particles.

PID consists of 24 EJ204 plastic scintillators arranged in cylindrical shape. Each scintillator strip is 500mm long and 4mm thick, and, in order to minimize the gaps between adjacent scintillators, the design demanded that they should have a right-angle trapezium cross-section. Each strip is wrapped in an aluminized Mylar foil in order to optically isolate the scintillation light. The scintillators are connected to different PhotoMultipliers (PMT), Hamamatsu R1635 and E1761-04 via perspex light guides. An aluminum ring with 24 holes supports the construction where the PMTs are positioned in order to match the arrangement of the scintillator strips (Fig. 3.8). The entire detector is wrapped in a black Tedlar foil to ensure the lightproof of the detector.

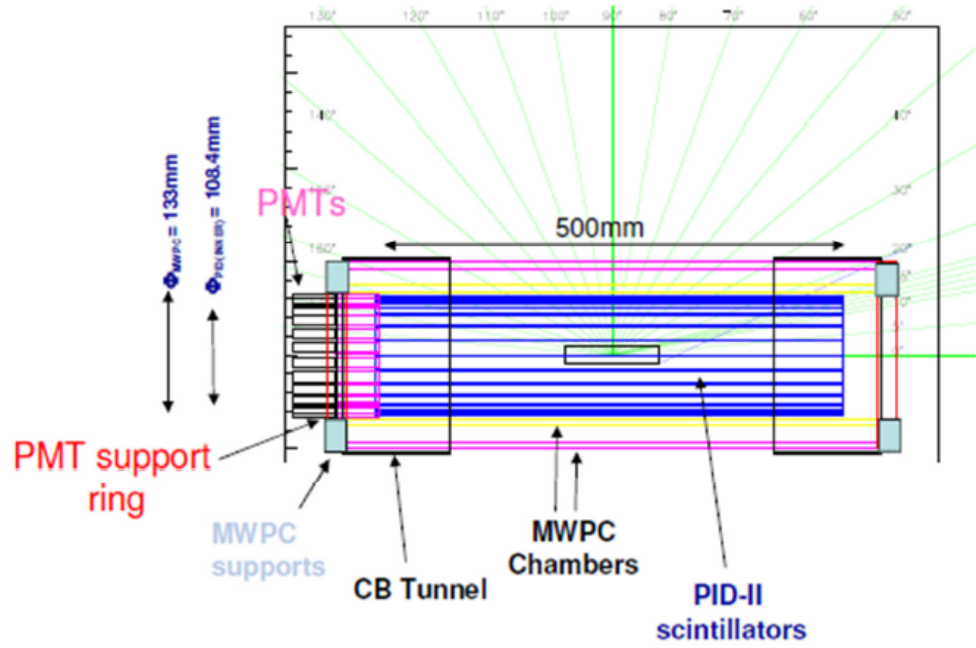


Figure 3.8: PID schematics.

The design of the PID allows for the full coverage of the azimuthal angle and for the coverage from 20° to 160° of the polar angle. This coverage matches exactly the parameters of the CB. When a charged particle passes through the scintillator it deposits a fraction of its energy while the rest of its energy will be detected in the Crystal Ball. The identity of such particle is determined by correlating the events from both detectors while enforcing that the hit in the CB is within 15° from the center of the PID scintillator (azimuthal angle). When plotting the energy deposited in the PID against the energy registered in the CB on a two-dimensional plot a characteristic shape is obtained (Fig. 3.9). The proton and pion distribution are easily identifiable in such a plot.

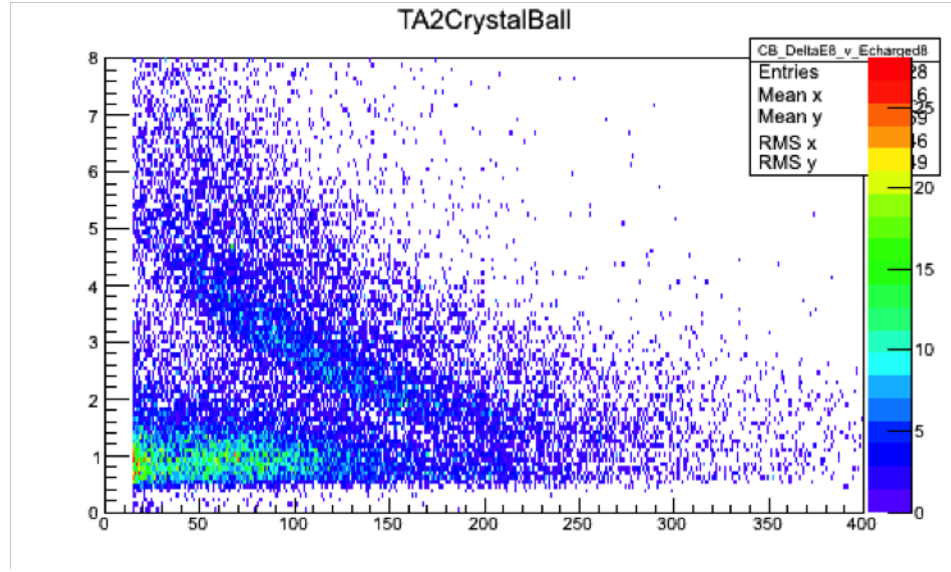


Figure 3.9: ΔE -E plots of PID and CB energy deposits.

3.7 TAPS

The Crystal Ball detector has been designed for colliding beam experiments: For this reason the detector doesn't cover $\sim 20^\circ$ in the polar angle range for both the backward and the forward direction. In order to fill this gap, another detector had to be added to the system: the TAPS detector. In MAMI, the CB is used for fixed target experiments. This kind of experiments are characterized by the fact that the reaction products are Lorentz boosted forward. For this reason it is crucial for many experiments that the additional TAPS detector covering those missing forward 20 degrees has been mounted [61].

TAPS is located 1.5m downstream from the reaction vertex. It is a segmented calorimeter detector made from 385 hexagonal BaF₂ crystals (Fig. 3.10). Each crystal is 25cm long, wrapped in 8 layers of 38 μ m thick UV-reflecting PTFE (Teflon) foil and a single layer of 15 μ m thick aluminum foil in order to assure light proofing. The cylindrical end part of each crystal is connected to an Hamamatsu R2059 PMT through silicone glue.

The barium fluoride crystals, even though have much lower scintillation output than the NaI crystals used in CB, have higher density (4.89g/cm³) and larger atomic number. These characteristics provide just as good detection efficiency.

Another key property of the BaF2 crystals over other materials is their fast timing resolution ($\sim 0.6ns$), which makes the detector ideal for identifying particles through time of flight (TOF) methods [61].

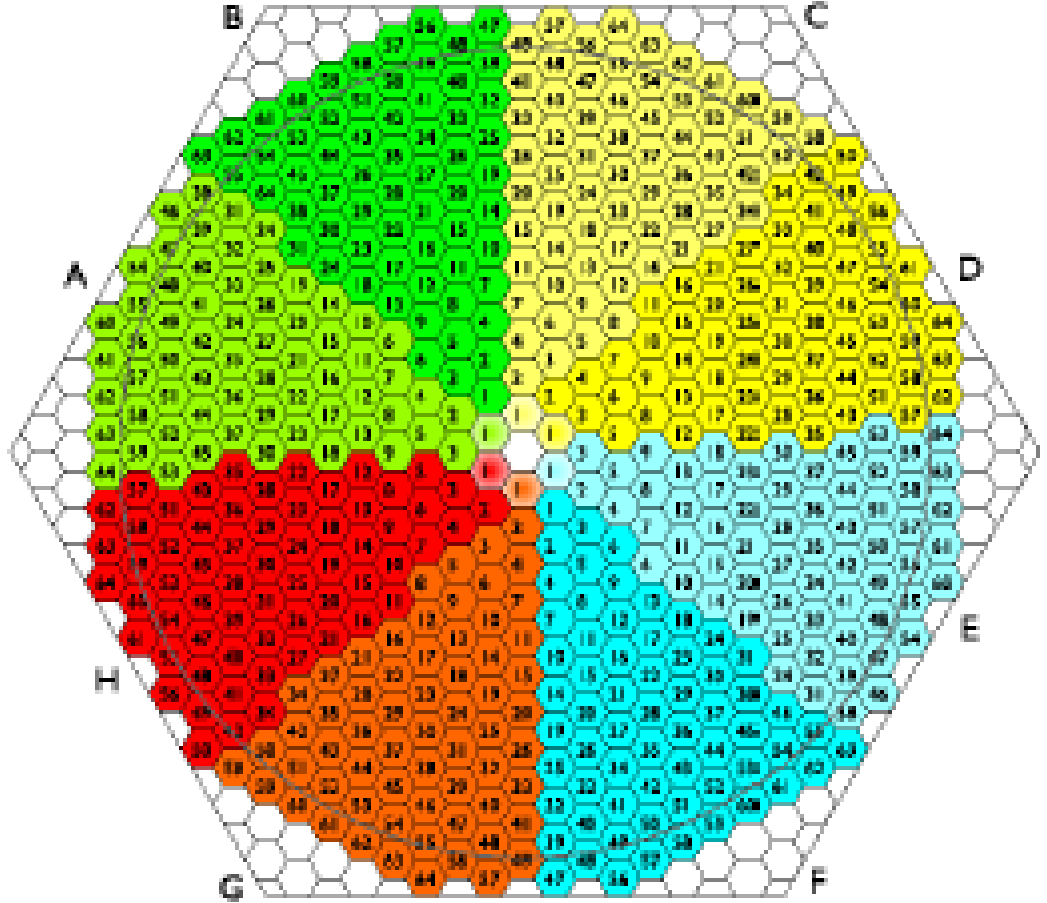


Figure 3.10: Diagram of the BaF2 crystals arrangement in TAPS. Different colors represent sectors that can be used in the trigger if required.

Directly in front of TAPS, there is an array of 5mm thick NE102A plastic scintillators which constitute the TAPS Veto detector. The output from this detector is collected by optic fibers in Valvo XP2972 phototubes. This addition to TAPS allows the discrimination between neutral and charged particles by correlating events from TAPS Veto and TAPS. This allows charged particles to be identified as a function of their energy and energy deposition.

As mentioned before, a parallel method used by TAPS in order to identify particles is through the time of flight of the particles. By measuring the time used by a particle to travel from the target to the TAPS detector one can discriminate between higher mass particles (like protons and neutrons) and particles traveling at or almost at the speed of light like photons and electrons.

A different method of particle identification, the pulse shape analysis, exploits the fact that BaF2 crystals have fast (0.6ns) and slow (620ns) decaying components. Each particle type leaves its own particular imprint on slow and fast components and by comparing the ratios of energy deposited in both, it is possible to improve the particle identification process.

3.8 Targets

A previously performed experiment of coherent π^0 photoproduction on ^{208}Pb target confirmed the existence of the neutron skin. However, in order to confirm the conclusions of that measurement it was desirable to repeat the experiment with another heavy nuclei. Furthermore, it has been shown that establishing the evolution of the neutron skin along an isotopic chain promise better results to put tighter constraints on the parameters of the neutron rich matter equation of state [38].

The targets used in this experiment were three isotopes of tin (^{116}Sn , ^{120}Sn and ^{124}Sn); chosen because of its stability, and because these elements easy of availability. Theoretical calculations predict a change of 0.05 to 0.15fm in the neutron skin thickness when going across the isotopic chain of tin from ^{116}Sn to ^{124}Sn (Fig. 3.11) [37]. Measuring the skin thickness across the isotopic chain cancels out any systematic error, and therefore, allows to accurately measure the changes predicted by the models.

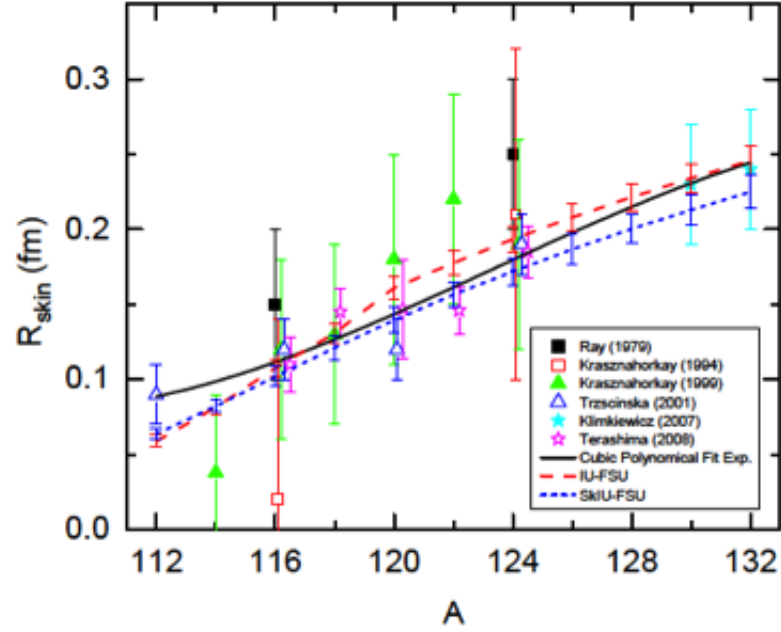


Figure 3.11: Predictions of neutron skin thickness for tin isotopes from the IU-FSU and SkIU-FSU models.

The targets were secured in a target holder and placed inside a PVC tube at the center of detectors. The details of the targets are given in the below table.

Table 3.3: Tin targets

Isotope	mass (<i>MeV</i>)	thickness (<i>mm</i>)	density (<i>g/cm</i> ²)	surface density (<i>nuclei/cm</i> ²)
¹¹⁶ <i>Sn</i>	107961.738	1.0	7.14	3.7104×10 ²¹
¹²⁰ <i>Sn</i>	111688.180	0.5	7.38	1.8535×10 ²¹
¹²⁴ <i>Sn</i>	115417.416	1.0	7.63	3.7089×10 ²¹

3.9 Data Acquisition

The analogue output signal of the detectors' PMTS has been read out and translated into a digital signal by the data acquisition system (DAQ) with the

use of charge to digital converters (QDCs), analogue to digital converters (ADCs) and time to digital converters (TDCs). The latter measures the time difference between the start signal of an experimental trigger and the stop signal from a given detector element, thus provided the information about the time of the event. The ADCs give digital information proportional to the pulse height of the signal, while QDCs return digital signal proportional to charge; both these values, pulse height and charge are proportional to the energy deposited in the detector element. ADD MORE THINGS. READ IT AGAIN... a little more than we use a bunch of QDC, ADC and TDC for the DAQ.

3.9.1 Tagger Electronics

The energy of the bremsstrahlung photons was obtained from the hit position of the recoiling electron on the tagger focal plane. The timing of such hit was used to match the events in the detectors with the hits on the focal plane. Providing that the a signal from the focal plane passed the threshold of the discriminator, a logic pulse was fed to a Compass Accumulation, Transfer and Control Hardware (CATCH) TDC (section 3.8.2) to record the time of the hit. Simultaneously, a signal from the discriminator was sent to FASTBUS scalers, which provided the count rate for each FP detector element. This was subsequently used to determine the photon flux.

3.9.2 Crystal Ball Electronics

As depicted in (Fig. 3.12), signals from each PMT are sent to fan-out units splitting the analogue output into three signals. One passes to a Flash ADC (F-ADC) via a delay, second goes through the discriminator and branches to a scalar and CATCH TDS. And the third signal is fed to the triggering electronics.

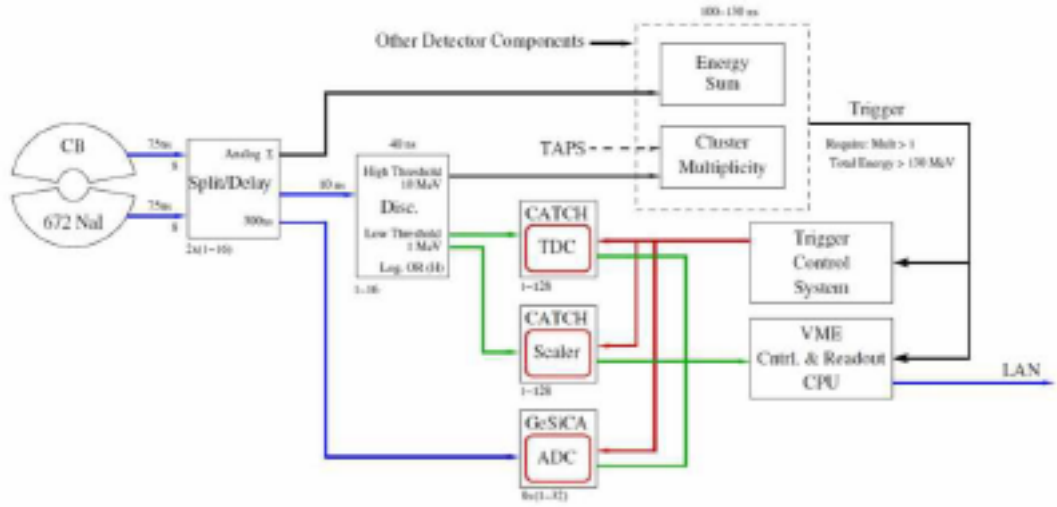


Figure 3.12: Crystal Ball electronics [51].

The integral of the pulse from each PMT was obtained from the F-ADCs, which sampled the shape of the signal with a frequency of 40 MHz. Since the DAQ was not prepared to handle such large volumes of data, only the integrals of pulses over three regions were taken. The integration is done over a time window of 750ns (30 signals). The first window was set to sample the pedestal whose signal is a convolution of remnant light and residual charge in the PMTs. The second window was set over the signal, and the third was set to evaluate the tail of the pulse. This set up allowed for the simultaneous measurement of the signal and the pedestal for every event, and with the dynamic subtraction of the pedestal from the signal, the energy resolution of the crystals could have been significantly improved.

Contrary to the typical TDCs, which are started by a hit in a relevant detector and stopped by a logic pulse from the trigger, CATCH TDCs, developed for the Compass experiment at CERN, allow for multiple hits in TDCs [30]. Using a 10GHz oscillator each TDC is running independently while the CERN-standard trigger control system synchronizes the signals in those TDCs. One of the TDCs is designated as a reference element and attached to the trigger. When an event passes the trigger threshold a logic pulse is sent to this reference TDC and the oscillator value is stored. When other TDCs record a hit, corresponding oscillator

value is stored in a buffer. In order to extract the information on the timing of an event the oscillator value stored in the reference TDC has to be subtracted from the oscillator values recorded by other TDCs, the conversion rate of 117 ps/channel is then used [70].

3.9.3 TAPS Electronics

The signals from the TAPS PMTs received similar treatment to those from Crystal Ball and were also split into three separate signals. One signal was directed to a TDC via a constant fraction discriminator (CFD), which analyzed the shape of the pulse and provided accurate timing information for the QDCs. The other two signals were fed to separate QDCs, one with integration time of 40ps, other with 200ps, this double integration allows for a pulse shape analysis.

3.9.4 Triggering Electronics

While the event is being registered by DAQ, no other event is being recorded; this is defined as dead time. In order to reduce the effects of the dead time, a series of triggers were set up to limit the events read by DAQ only to those relevant to the experiment. Two LeCroy LRS 4805 logic units were used to define the conditions an event must satisfy in order to be recorded.

The first level trigger for this experiment required the sum of energy deposited in all 672 NaI crystals to be greater than 40MeV. For the second level trigger, DAQ grouped NAI crystal into clusters of 16, and it was required that there were two hit clusters detected in the CB. When those two conditions were satisfied DAQ read the event and reset the electronics.

3.10 Analysis code

Online analysis and monitoring of the data have been done using the AcquRoot framework. AcquRoot has been written in C++ specifically for the data analysis at MAMI, it uses libraries and tools of ROOT [9, 15]. AcquRoot consists of three components, AcquDAQ Data Acquisition, AcquRoot Analysis and AcquMC Event Generator.

Offline analysis was done using the a2GoAT framework(A2 Generation of Analysis Trees). In this framework AcquRoot is used to produce analysis trees containing only basic track information. The GoAT software package is then used to process those trees; here particle reconstruction, all the data checks and sorting is performed.

Chapter 4

Calibrations

This chapter addresses the calibrations of all the detectors. The process involved converting raw signals from the detectors into real physical quantities allowing for the energy, position and timing corrections to be determined and applied in the subsequent analysis.

4.1 Tagger Calibrations

4.1.1 Energy Calibration

The tagger energy calibration determines the relation between tagger channel number and electron energy. The calibrations were carried out by the colleagues at the University of Glasgow [56].

In order to make a tagger energy calibration, an incident MAMI electron beam of an energy of interest is bent in the magnetic field; for a 855MeV beam, field of 1.025T is used. Then the magnetic field was varied in small steps to guide the beam through the focal plane and an energy measurement was taken at each step. Six different electron beam energies were used for the calibration, they ranged from 195.22MeV to 705.26 MeV, with the uncertainty of 0.16MeV; the uncertainty in the magnetic field was 0.01mT [58].

The varying magnetic field required to sweep the beam across a given channel allowed for the determination of a position of a hit in a FP detector with an accuracy of 0.05 channel width. Finally, in order to relate the the FP channel number to the electron energy a linear interpolation between different energies

was used.

4.1.2 Random Subtraction

Some of the hits in the tagger do not correspond to the photon-triggered reactions in the target. Those hits contribute to the background due to the bremsstrahlung electrons that produced photons, which passed the target without any interactions, Moeller scattering in the radiator (non-radiative reactions) and photons which were removed from the flux by the collimator. They are known as *random* hits, in contrast to the *prompt* hits, which correspond to the photons that triggered reactions in the target. In order to discern which tagger hits should be classified as prompt and which as random the timing analysis of the events have been carried out.

The time recorded by the tagger TDCs for each element in the focal plane is a measure of the time difference (time taken by the photon to reach the target plus the time taken by the photon-induced reaction products to satisfy the experimental trigger) between the hit in the tagger detector elements and the experimental trigger (Fig. 4.1). The hits in the tagger that correspond to the photons triggering reactions in the target form a prompt peak in the tagger time spectra. The peak is a reflection of the fact that for prompt hits will have a roughly constant time difference. On the other hand, the electron hits which did not correspond to the photons triggering the reactions within the target result in a flat background of random hits in the time spectra.

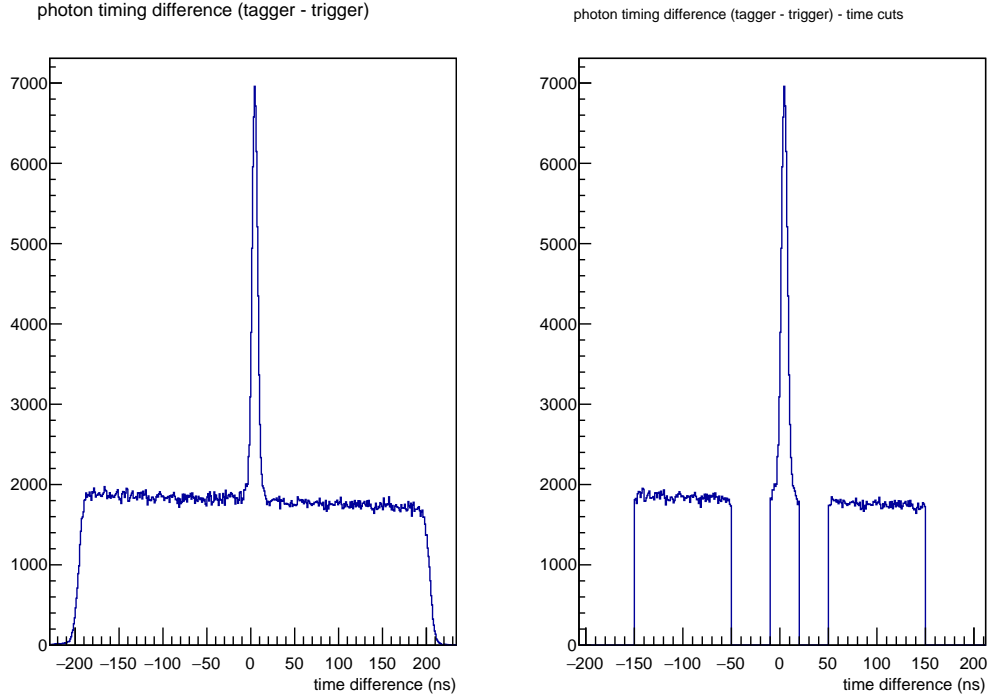


Figure 4.1: Time spectrum of the hits in the tagger. The plot on the left shows the full time spectrum and the plot on the right shows the cuts defined for the prompt and random regions.

Nevertheless, it is not possible to categorise hits as prompt or random for an individual event because there is still some random contribution to the prompt peak. In order to resolve this, a large number of events have been recorded and an appropriately weighted (to account for the different size of prompt and random regions) sample of the random hits have been subtracted from the prompt hits.

It must be noted that the timing cut used to define prompt and random regions have been done after tagger timing alignment have been done. Only then all the tagger detector elements had the prompt peaks aligned and the time cut could have been applied.

4.2 Crystal Ball Calibrations

4.2.1 Clustering Algorithm

Photons entering Crystal Ball deposit their energy in the NaI crystals via electromagnetic showers which hit multiple crystals in each event. These groups of hit crystals are called clusters. The accurate analysis of the CB events required an algorithm which identifies the clusters and recovers information about the incident photon's energy and position from the energy deposited in the crystals within a cluster.

First step in the analysis is to identify a crystal with the highest energy deposit, central crystal of the cluster, and it's 12 closest neighbors (Fig. 4.2). A hit in this central crystal provides the timing information for the event. The energies of the neighboring crystals are scanned and if their energies are greater than the threshold energy of around 2MeV they are added to the cluster. Only 12 closest neighbors of the central crystal are considered in the algorithm because it has been confirmed that in 98% of the cases the energy deposit of the shower triggers only 13 crystals [73]. Then the total energy of the cluster is obtained as:

$$E_{sum} = \sum_k E_i \quad (4.1)$$

where, E_i is the energy of the i-th crystal in the cluster of k detector elements. Then the condition of the the total energy of the cluster being greater than 20MeV is applied to suppress the effects of the background.

The position of the hit is calculated as the weighted mean position given by the below equation:

$$r_{mean} = \frac{\sum_k \sqrt{E_i} r_i}{\sum_k \sqrt{E_i}} \quad (4.2)$$

where, E_i is the energy deposited in the i-th crystal and r_i is the position of the i-th crystal in the cluster.

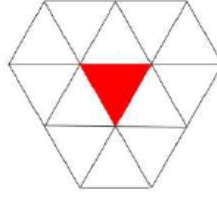


Figure 4.2: Schematic representation of a NaI cluster. The central triangle, shaded in red, depicts a triangular face of the NaI crystal and is the logical center of the cluster. The other 12 triangles are its closest neighbors.

4.2.2 Energy Calibration

Crystal Ball energy calibrations have been carried out by the colleagues from UCLA and Johannes Gutenberg University in Mainz [75]. The energy calibration of the Crystal Ball was performed in three steps; a low energy calibration - mainly important for the acquisition system was obtained, then a high energy calibration has been performed, and in the end, an energy scale factor has been applied to account for crystal thresholds and clustering algorithms.

4.2.2.1 Low energy calibration

In this first step of the CB energy calibration, an $^{241}\text{Am}/^9\text{Be}$ source was placed in the center of the Crystal Ball [75]. The α decay of americium, and a subsequent capture of these particles by beryllium, triggers a series of reactions resulting in the excited state of ^{12}C which decays to a ground state and emits a 4.438 MeV photon in the process. This photon energy deposit in the NaI crystals has been used to adjust the gains of all PMTs, so that the detected peak was in the same position in the ADC spectra for all the detector elements.

4.2.2.2 High energy calibration

The photons produced in meson decay have energies much higher than photons used in the low energy calibration, therefore the calibration for higher energy photons is also required. The $\pi^0 \rightarrow \gamma\gamma$ reaction have been used as a source of such photons. The invariant mass, $M_{\gamma\gamma}$, of two photons detected in the CB was reconstructed from the information on the photons measured energy and

momentum and only the events with $M_{\gamma\gamma}$ within the mass of π^0 were selected, and the following selection cuts have been applied:

- no less than 70% of the detected photon energy had to be deposited in a single NaI crystal. This criterium was decided upon to ensure the deposit in a single crystal dominated the cluster.
- in order to ensure that the photons used for the calibration were of similar energy, the condition of having the energy difference between two photon clusters being less than 35% of the total energy have been set up.
- the tagged photon energy had to be less than 180MeV. This restriction constrained the energy range of the decay photons between 40MeV and 125MeV. Such energy cut favored large opening angles between the photons, resulting in an even angular distributions in the lab.

The invariant mass of π^0 has been reconstructed from the two photon decay, and a Gaussian function has been fitted. The mean of the fit, corresponding to $M_{\gamma\gamma}$, has been compared to the mass of π^0 . With this information a new gain factor, G_{new} , was obtained according to the below equation:

$$G_{new} = \frac{M_{\gamma\gamma}}{M_{\pi^0}} G_{old} \left[\frac{MeV}{channel} \right] \quad (4.3)$$

where, G_{old} is the gain factor used previously. Because the detected energy of the photon cluster depended both, on the central crystal and all the other crystals in the cluster a single set of calculation to obtain the new gain was not enough. Several iterations were required for $M_{\gamma\gamma}$ to correspond to M_{π^0} .

4.2.2.3 Energy scaling factor

Because of the energy losses due to individual energy thresholds and the showers, the energy of the incident photons is not the same as the total energy of the cluster. To account for this in the analysis, another energy correction had to be applied. In order to ensure that the mass reconstructed from the decay of two photons was indeed the mass of π^0 meson, a scaling factor of 1.05 was applied to the data.

4.2.2.4 Time walk correction

Because of the slow time response of the NaI crystals, 250ns [50], there arises a time difference between the small and large signals registering at the discriminator threshold. Therefore, the times reported by the TDCs required a correction to account for this time difference and therefore improve the CB time resolution (Fig. 4.3). The corrected time, T_{corr} , is defined as:

$$T_{corr} = T - r \sqrt{\frac{a_0}{a}} \quad (4.4)$$

where, T is the measured time, a_0 is the discriminator's voltage, r is the rise time and a is the signal's amplitude.

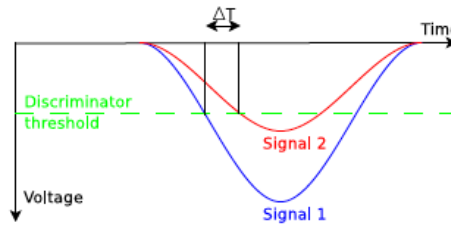


Figure 4.3: CB time walk.

4.3 PID Calibration

4.3.1 PID azimuthal correction

In order to accurately determine the correlation between hits in the PID and Crystal Ball, the PID azimuthal angle (ϕ) with respect to the Crystal Ball had to be measured. The steps taken to calculate the value of phi are as follows.

First, only the events that triggered signal in one crystal in a CB cluster were selected. The reason for that was to limit the number of photons producing events in more than one crystal and therefore, ensure that only events with clearly determined angles were considered for the calibration. Another cut was made on those events to select only those with just a single reaction in the PID. This way the background due to multi-body final state interactions was highly

reduced. The angular distribution of those events has been plotted for each PID element, which gave a single peak over the azimuthal range of each one (Fig. 4.4). A 1D projection has been plotted for each PID element and a Gaussian function was fitted to the peak. Having 24 PID elements means that each of them occupies 15deg of the total azimuthal coverage. Therefore, a linear fit with a fixed gradient could have been used to accurately determine the PID azimuthal correction (Fig. 4.5).

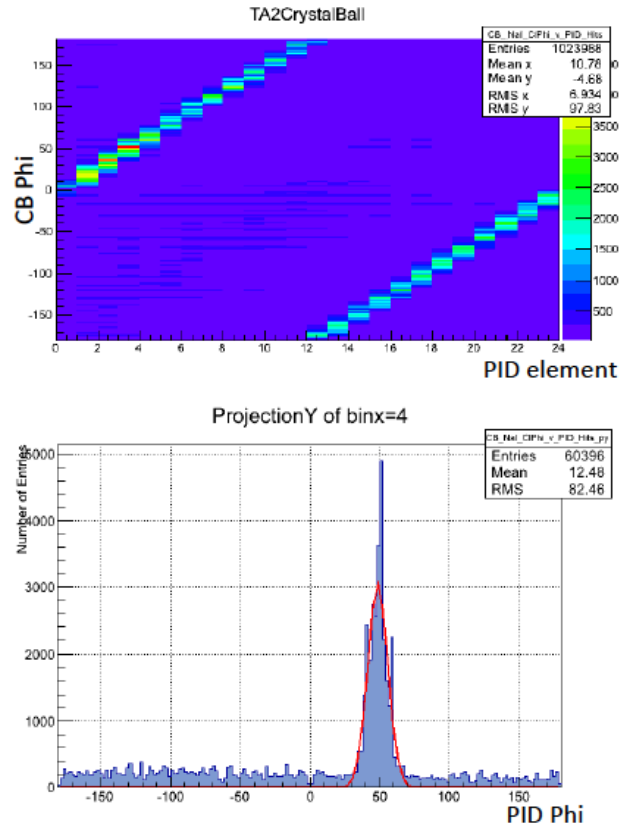


Figure 4.4: Plot of Phi position in CB cluster vs hit in PID (top) and Gaussian fit to the projection of PID element 4 over the azimuthal range (bottom).

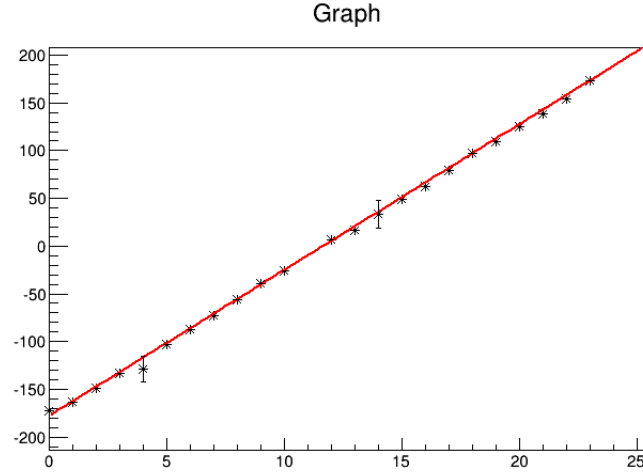


Figure 4.5: PID azimuthal correction - linear fit.

4.3.2 PID energy correction

The energy calibration employed banana (ΔE - E) plots described earlier and raw signal from PID ADCs. The banana plots were divided into 10MeV energy bins and projected onto the y-axis (Fig. 4.6). Those projections featured two peaks, first one corresponding to the pion and second one representing proton ridges. The latter was fitted with a Gaussian function and the value of the mean has been extracted (Fig. 4.7). This step has been performed for all the energy bins in the range of 20-300MeV. Similarly, the G4 simulated data had the same procedure applied. Subsequently, the means of the Gaussian functions for the experimental data have been plotted against corresponding means for the simulated data and a linear fit has been used to determine the gain for the calibration (Fig. 4.7).

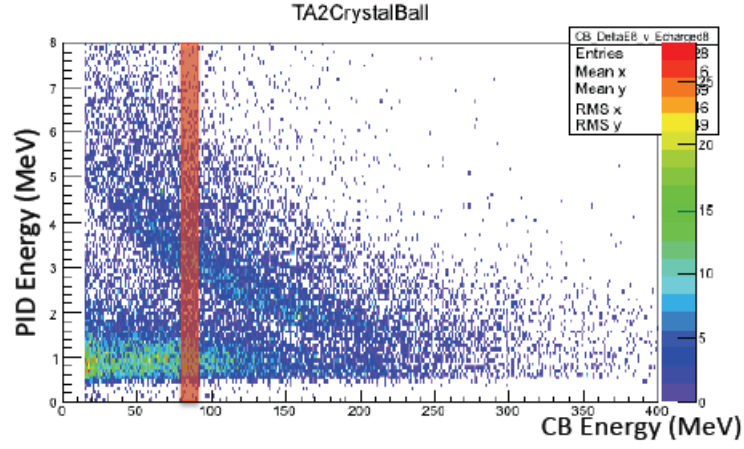


Figure 4.6: ΔE -E plots of PID vs CB energy deposits. Example, 10MeV energy bin shaded in red.

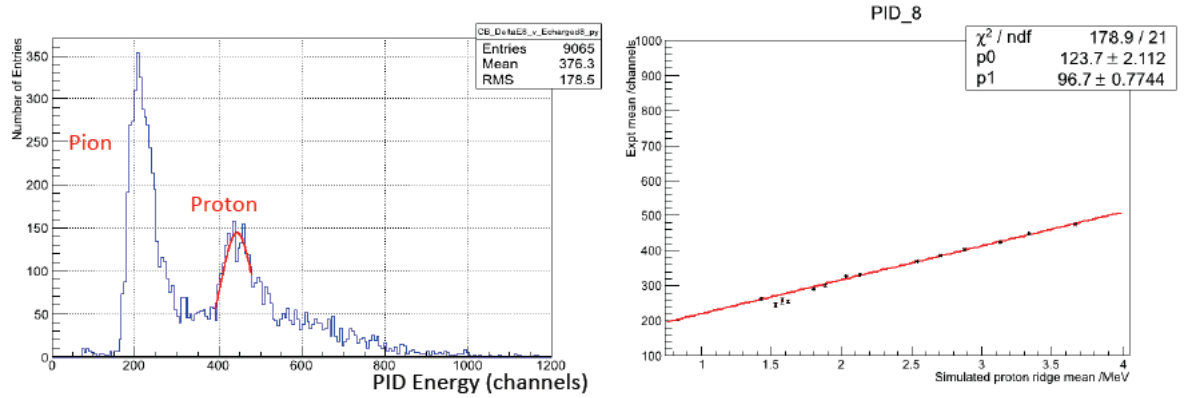


Figure 4.7: Gaussian function fitted to the proton peak (left) and linear fit to the Gaussian means (right).

The offset for the calibration has been obtained from the analysis of the raw ADC signal for each PID element. The first peak in the ADC spectrum (Figure 6) represents the pedestal position. A Gaussian function has been fitted to this peak and the value of the mean has been determined. This value is equivalent to the offset for the calibration.

4.3.3 PID time calibration

Accurate information about timing of the events, obtained with the TDCs, is essential part of the data analysis. Timing coincidence allows for correlation of coincidence particles between different detectors; it is used in clustering algorithm of the Crystal Ball, and enables particle identification in TAPS, therefore allowing for the association of a hit in FPD with an even in CB/TAPS detectors. The principles followed for time calibration of the various detectors are the same, therefore, only PID time calibration will be described in more detail below.

The TDC spectrum of each PID element was fitted with a Gaussian and a value of the means for all the elements have been extracted (Fig. 4.8). These values have been used to determine the offset in the calibration and align the peaks of all the detector elements in the timing spectrum (Fig. 4.10). The misalignment for the PID element 17 is caused by the malfunctioning PID element (Fig. 4.9).

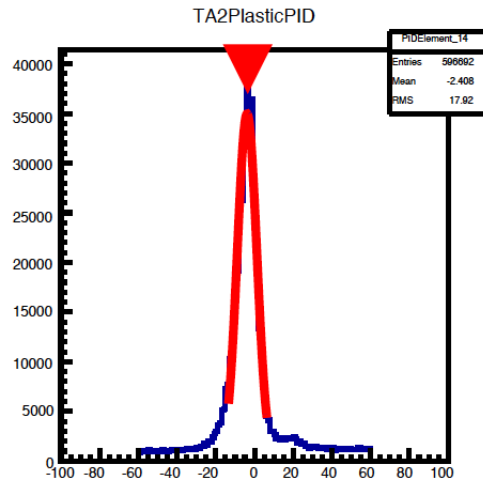


Figure 4.8: Gaussian fit to PID-element 14.

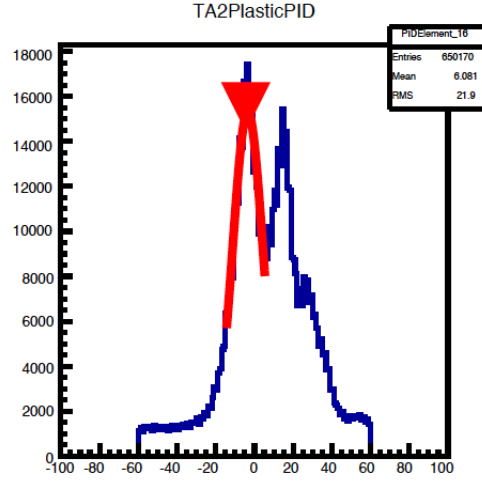


Figure 4.9: Gaussian fit to PID-element 16. The TDC spectrum of the malfunctioning PID element.

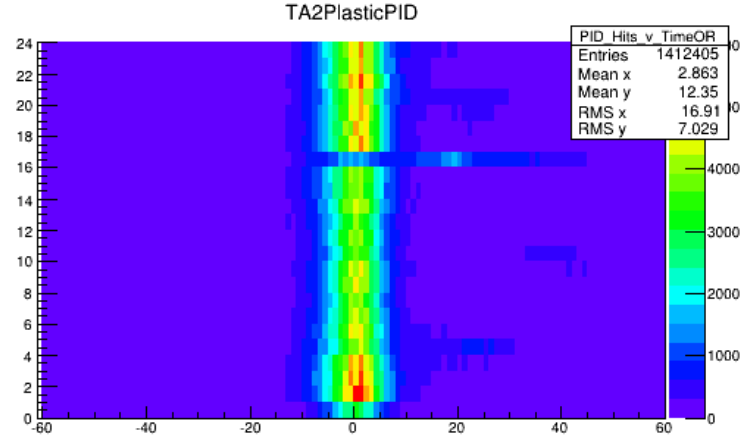


Figure 4.10: Time alignment of all PID elements.

4.4 TAPS Calibration

The calibration of the TAPS BaF₂ crystals employed cosmic rays using the mean deposited energy of the minimum ionizing muons equal to 37.7MeV [69]. For each of the BaF₂ crystals' PMTs the position of the energy peak has been adjusted

so it was at the same ADC position for all detector elements, and the channel number corresponding to the mean peak position was determined.

Using a similar technique to that employed in the CB calibrations, the correction for the gain was obtained. However, because detection of two photons from the π^0 in TAPS is very rare, the events having one photon detected in TAPS and one in CB were chosen. Detailed procedure of this calibration can be found in [52].

The procedure to calibrate plastic Veto was similar to the one used to calibrate PID. The pedestal positions were obtained from the raw ADC spectra and the gain was determined by comparing the experimental mean position of the proton peak in the Veto to the simulated data. Details of this method can be found in reference [47]

Chapter 5

Data Analysis

5.1 Target Position Correction

The information obtained from the MWPCs has been used to accurately determine the positions of the targets. The reaction vertex has been obtained from the analysis of charged tracks which come from the reaction of the photon with the target. The results of this reconstruction are presented in the below figures:

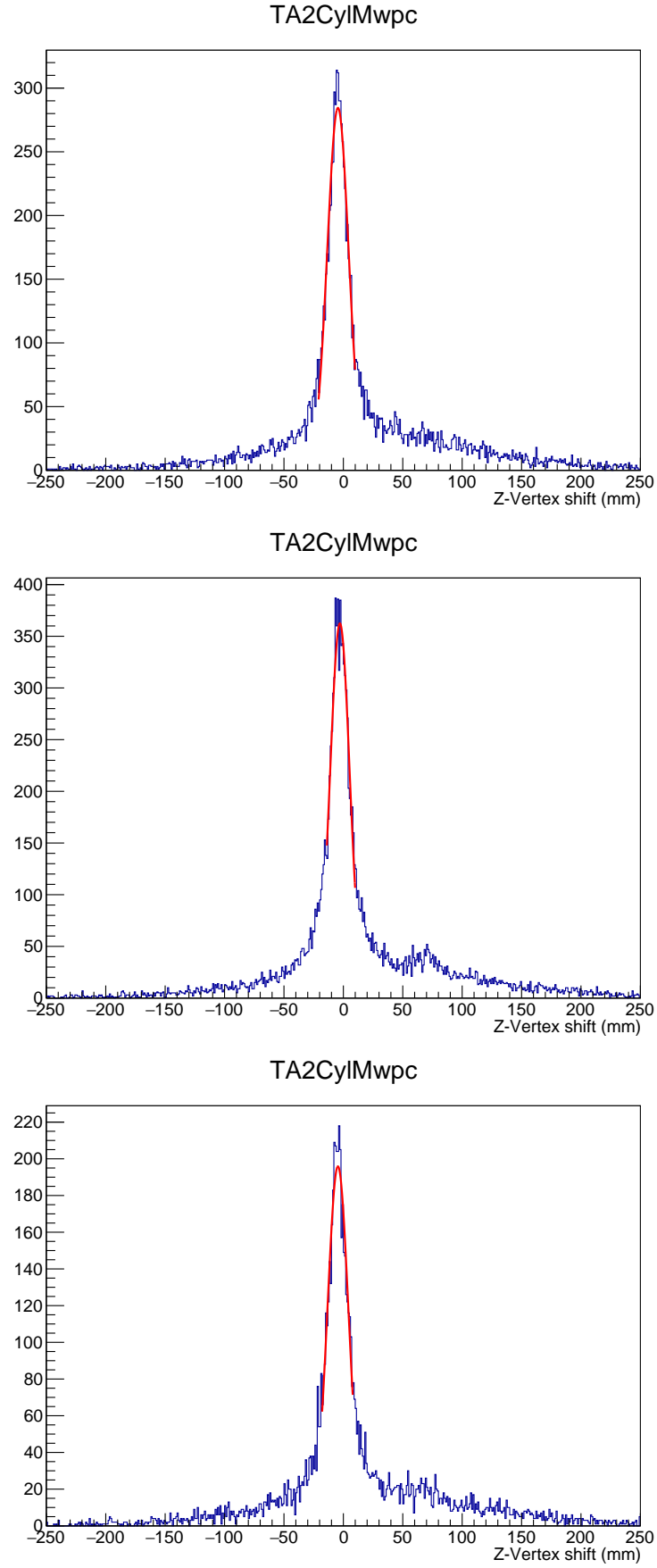


Figure 5.1: Target positioning. Top graph shows the fit results for the correction for ^{116}Sn , middle graph shows data for ^{120}Sn , and the bottom graph shows the fitted offset for ^{124}Sn .

The position of the target has been determined with the use of a Gaussian fit to the charged particle reaction vertices (Fig. 5.1). The mean of the Gaussian fit have been extracted and its value employed in the analysis as the target position correction.

The obtained value of the position offset with respect to the Crystal Ball have been used in the analysis code to correct the momenta of the detected particles. The below formulas show how the momentum is calculated for the target located in the centre of the Crystal Ball (Equation 5.1) and how the calculation is corrected when the effect of the position offset is included (Equation 5.2):

$$p = \frac{E_{meas}}{\sqrt{x^2 + y^2 + z^2}}(x, y, z) \quad (5.1)$$

$$p = \frac{E_{meas}}{\sqrt{x^2 + y^2 + (z - z_{corr})^2}}(x, y, z - z_{corr}) \quad (5.2)$$

where, E_{meas} is the measured energy of the deposit in the cluster, x , y , and z are the coordinates of the centre of mass of the cluster and z_{corr} is the correction due to the target position offset determined with the MWPCs.

The correction of the target z-vertex position has a direct effect on the calculations of reconstructed π^0 scattering angle θ . By default, the event reconstruction assumes that the target position is exactly at the centre of the Crystal Ball, including the target position correction shifts the reaction vertex upstream and gives more accurate calculations of the reconstructed pion scattering angle.

5.2 Coherent Events

As described in chapter 2, the π^0 photoproduction can occur in several of ways, and alongside the coherent process, incoherent and quasi-free reactions take place. In order to extract the coherent events from the background, missing energy analysis has been performed. This technique uses information on incident photon energy from the tagger and π^0 4-momentum reconstructed from the information recorded in the Crystal Ball.

The pion missing energy is calculated with the following formula:

$$\Delta E_\pi = E_\pi^{CoM}(E_\gamma) - E_\pi^{CoM}(E_{\gamma_1\gamma_2}) \quad (5.3)$$

where $E_\pi^{CoM}(E_\gamma)$, defined in equation 5.4 is the pion energy in the pion-nucleus centre of mass frame of reference. E_γ is the incident photon energy, s is the invariant mass of the photon-nucleus system and m_π and M^2 are the masses of pion and the nucleus respectively. $E_\pi^{CoM}(E_{\gamma_1\gamma_2})$ is the, Lorentz-transformed to the CoM reference frame, detected pion energy.

$$E_\pi^{CoM}(E_\gamma) = \frac{s + m_\pi^2 - M^2}{2\sqrt{s}} \quad (5.4)$$

Although the pion energy can be approximated as the sum of the energies of the two decay photons, considering the angular information of the reaction allows for much better energy resolution, and therefore, more accurate calculations [59]:

$$E_\pi = \sqrt{\frac{2m_\pi^2}{(1 - \frac{E_1 - E_2}{E_1 + E_2})^2 (1 - \cos\phi)}} \quad (5.5)$$

where, E_1 and E_2 are the detected energies of the two decay photons and ϕ is the opening angle between them. The Lorentz transformation of the detected pion energy to the CoM frame of reference is calculated with:

$$E_\pi^{CoM} = \gamma \left(E_\pi - \frac{E_\gamma}{E_\gamma + M} (E_1 \cos\theta_1 + E_2 \cos\theta_2) \right) \quad (5.6)$$

where, θ_1 and θ_2 are the polar angles of the two decay photons, E_π is the detected pion energy.

The condition for the coherent π^0 photoproduction process is satisfied when $E_\pi^{CoM}(E_\gamma)$ and $E_\pi^{CoM}(E_{\gamma_1\gamma_2})$ are the same. Background processes however, return negative values of ΔE_{pi} since the initial energy is split between other than π^0 particles produced in the reaction or used up to promote the nucleus to an excited state.

In order to extract the coherent π^0 yield the missing energy spectrum has been split into several energy bins in the photon energy range from 135 to 580 MeV, and initially into 180 angular bins in the θ_π range of $0 - 180^\circ$. The resulting spectra were then fitted with one or two functions describing the coherent and background signals.

The fitting procedure has benefited greatly from the existing knowledge about

elastic and inelastic cross sections. In the electron scattering experiments it has been already shown that elastic form factors peaks in the forward direction [72], from there it follows that the elastic cross sections will be forward peaked as well. For the incoherent processes, however, the form factor and so the cross section variation is much smaller across the pion scattering angular range [44]. This behaviour implies that for the coherent π^0 scattering regions, the ΔE_π spectrum will be entirely dominated by the coherent peak. This should allow to fit the coherent peak and determine its fit parameters with a high level of confidence. This fit information can be subsequently used for the fits in the regions where incoherent contributions dominate.

The first step in the fitting procedure was plotting the 2D spectra of pion scattering angle, θ_π against the pion missing energy, ΔE_π for the photon energies in the range of $E_\gamma = 135 - 580 \text{ MeV}$, an example plot is shown in Fig. 5.2.

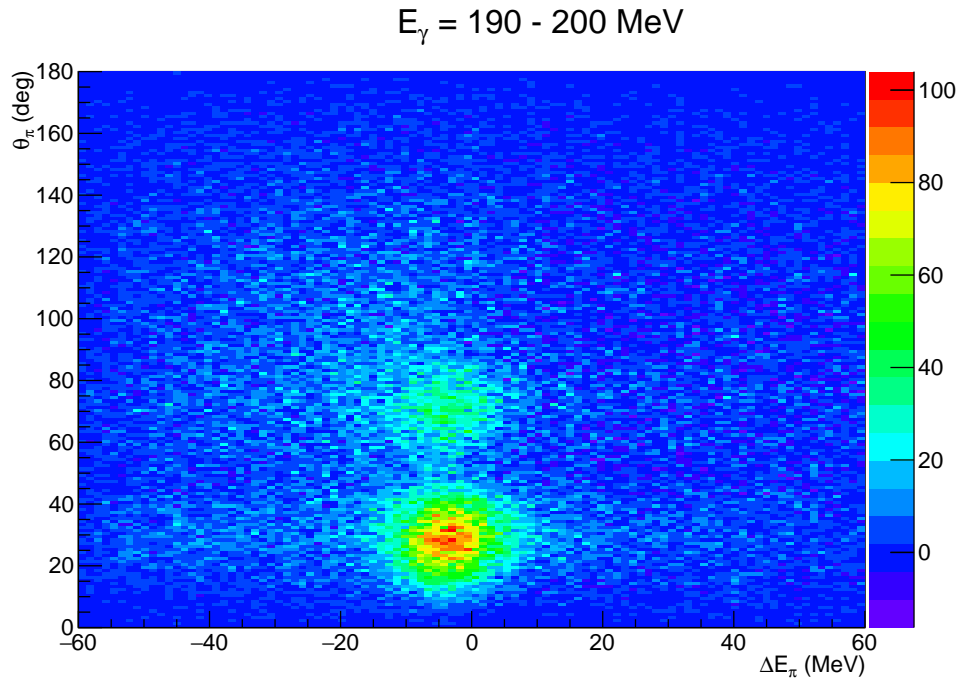


Figure 5.2: The plot of the pion scattering angle θ_π against pion missing energy ΔE_π for the ^{116}Sn data.

Next, the 2D spectra have been projected along the x-axis in 3° angular bins creating an array of one dimensional histograms. Then, nine projections around

the first diffraction maximum (the angular range of $15 - 36^\circ$) have been selected to fit the coherent signal with a Gaussian function. The width of the fit have been extracted and using this values to constrain the coherent peak a second iteration of fits has been performed. This time however, a fit function built from two Gaussian functions have been used to fit the data. The below figure shows the fits around the diffraction maximum and minimum.

The area of the Gaussian function fitted to the coherent peak has been also calculated and stored as a measure of the coherent yield of the reaction [26].

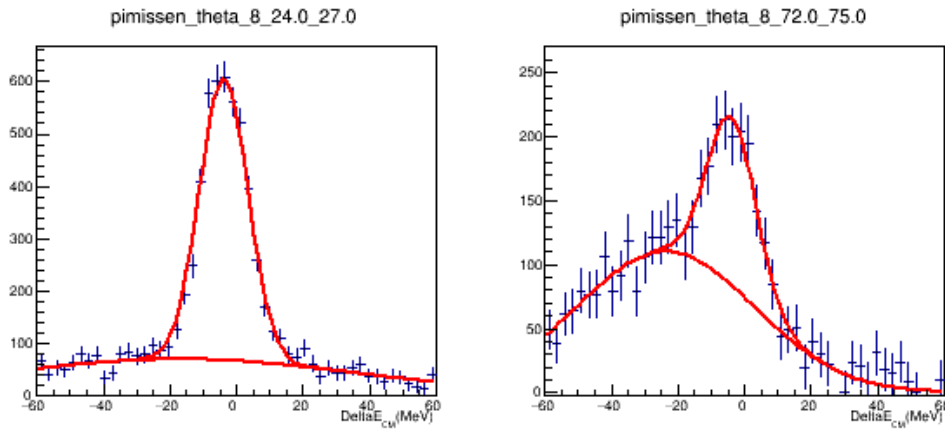


Figure 5.3: The fits to the pion missing energy spectrum for the energy bin $E_\gamma = 200 \text{ MeV}$. The graph on the left shows the fit around the first diffraction maximum, and the graph on the right shows the fit around the diffraction minimum.

The below plot shows the pion missing energy spectra after the background subtraction.

Figure 5.4: The plot of the pion scattering angle θ_π against pion missing energy ΔE_π for the ^{116}Sn data after the background subtraction.

5.3 Tagging Efficiency

A tagging efficiency measurements have been performed in order to accurately determine the beam luminosity, which is necessary for the π^0 yield normalisation in the cross section measurements. As described in chapter 3, the information about the photon flux is obtained from the number of hits in the FP detector. However, when the beam passes through the collimator further photons are removed from it and in order to account for this reduction in the flux a dedicated measurement with a lower beam intensity is performed.

The measurements have been taken for each target separately and the results are presented in the below figure (Fig. 5.5).

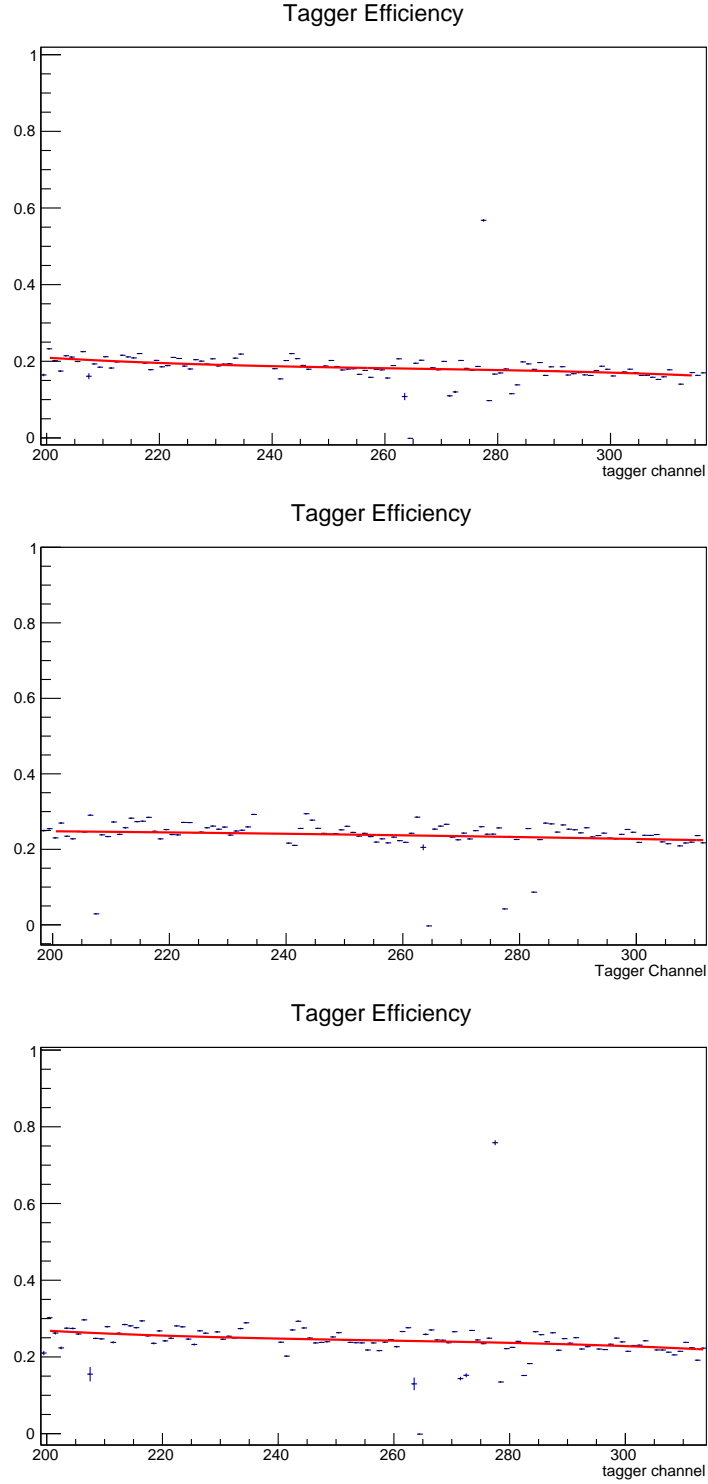


Figure 5.5: Tagging efficiency as a function of channel number for the tin targets. The top graph shows the results for Sn^{116} , the middle graph shows the results for Sn^{120} and in the bottom graph are results for Sn^{124} .

5.4 π^0 detection efficiency

A Geant4 Monte Carlo simulation has been used to calculate the efficiency of the detector setup.

In order to decrease the time required for the simulation, the minimum number of the generated events have been decided upon. This number was based on the analysis of the impact on the total error on detection efficiency (ϵ_{det}), which in turn depends on the error on generated and reconstructed events.

It has been calculated that the error on the reconstructed events in the coherent peak was $\sim 1\%$. Setting this value as the maximum error on detection efficiency, calculations to obtain a number of generated events such that the error on ϵ_{det} was no higher than the error due to reconstructed events have been done. They yielded a value of 10 millions.

The $A(\gamma, \pi^0)A$ events have been generated for the energy range of 135 – 540 MeV, for each target. Those generated events have then been used as the input of the Geant4 simulation. The resulting data have then been analysed with the same analysis software as the experimental data.

The detection efficiency has been calculated for each energy and θ bin as the ratio of the total number of detected π^0 's to the total number of π^0 's generated in that energy and θ bin.

The dependence of the detection efficiency on the angle is shown in the below figures. The points at the edges don't follow the polynomial fit because the distribution fluctuates on both sides of the point at the poles and without introducing ϕ discrimination it is not possible to improve on this.

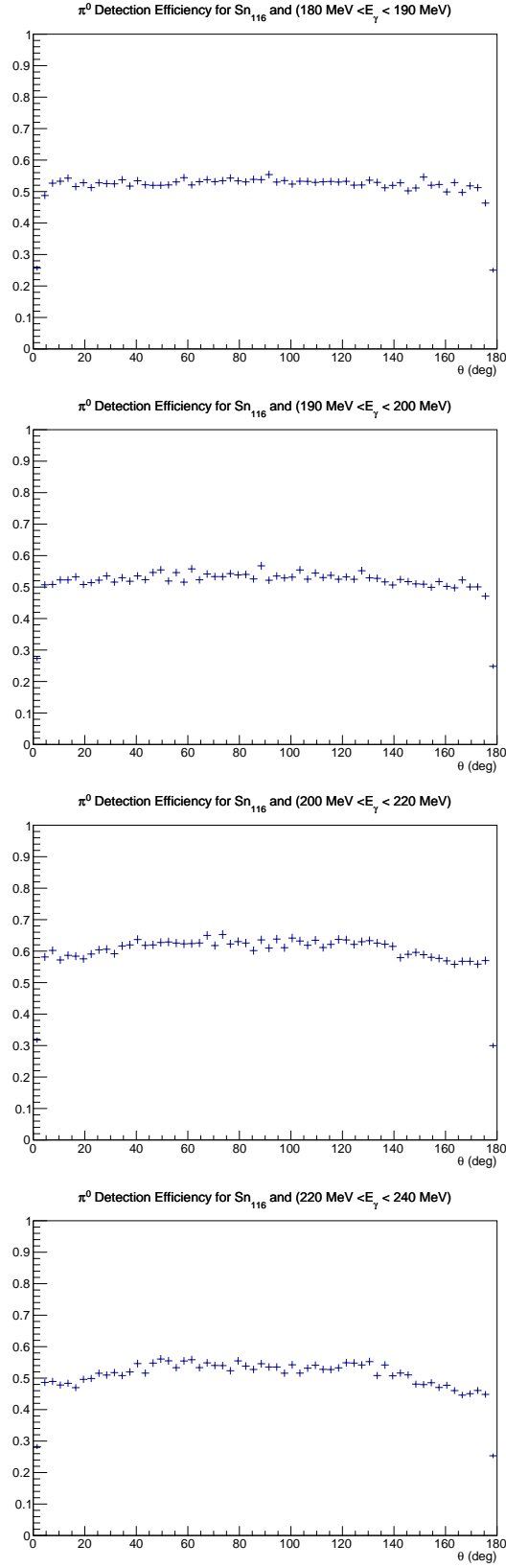


Figure 5.6: Dependence of the detection efficiency on energy and θ_{π^0} for the ^{116}Sn target.

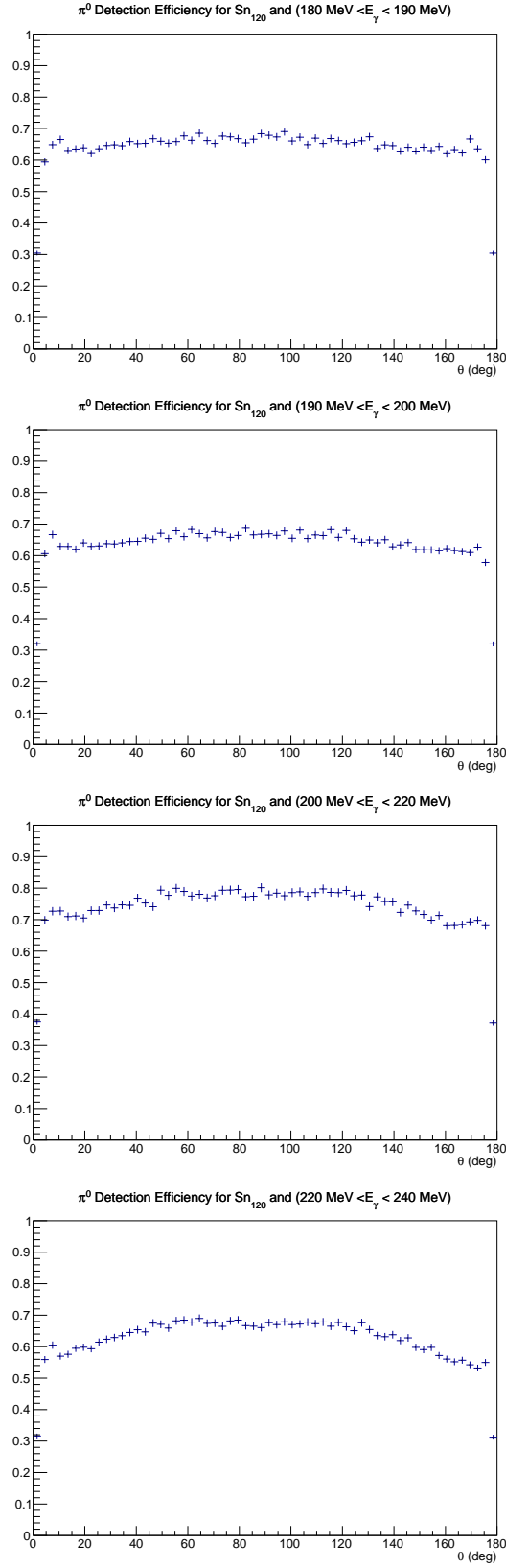


Figure 5.7: Dependence of the detection efficiency on energy and θ_{π^0} for the ^{120}Sn target.

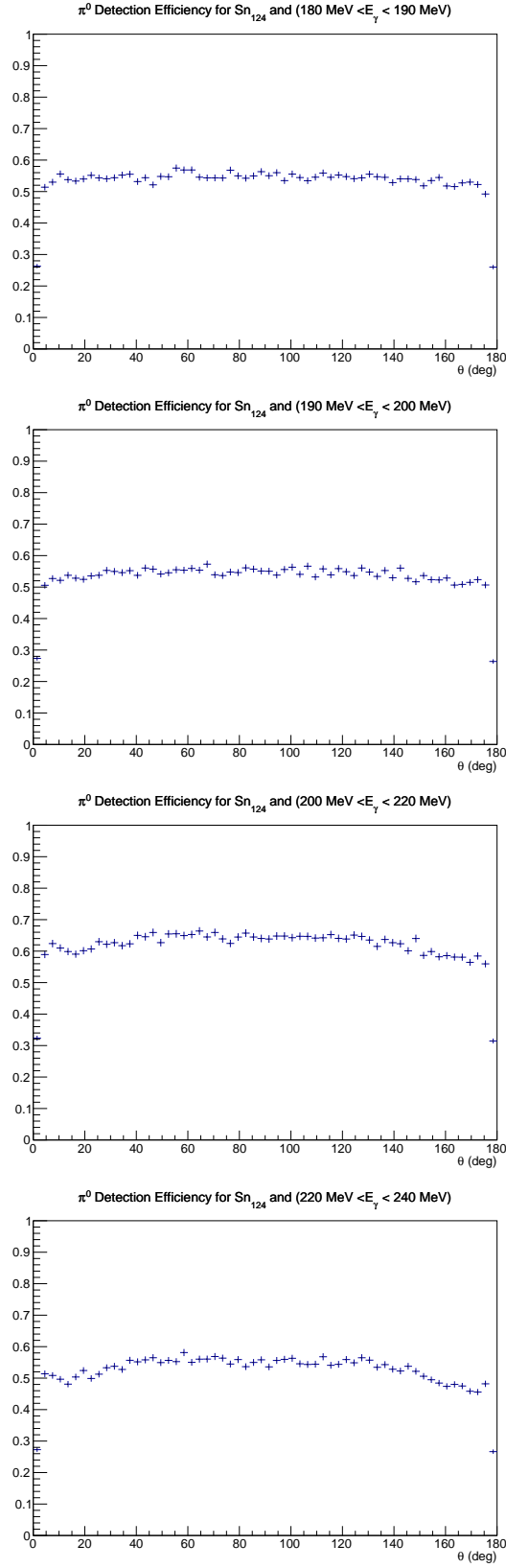


Figure 5.8: Dependence of the detection efficiency on energy and θ_{π^0} for the $^{124}\text{Sn}_{68}$ target.

5.5 Cross Sections Measurements

The measurement of the cross section is an important way to compare and contrast various theories with the experimental results. From the definition, cross section is a measure of probability that a certain reaction will take place under specified conditions. For a reaction $A(a, b)B$ is defined as:

$$\sigma = \frac{N_b}{N_a N_A} \quad (5.7)$$

where, N_a is the number of incident particles per unit area, N_A is the number of target particles per unit area visible to the beam and N_b is the number of emitted particles.

In this experiment, N_a is the incident photon flux calculated from the number of hits in the tagger scalers corrected with the tagging efficiency, N_A is the surface density of the target as seen by the beam, and N_b is the π^0 yield corrected with the detection efficiency.

The differential cross section is a derivative of the total cross section with respect to the solid angle. For a given photon energy bin, E_γ , and pion scattering angle, θ_{π^0} , it can be expressed as:

$$\frac{d\sigma}{d\Omega} = \frac{N_{\pi^0}}{N_s \epsilon_{tagg} \epsilon_{det} \rho_a \Omega \Gamma_{\gamma\gamma}} \quad (5.8)$$

where, N_{π^0} is the number of π^0 's detected in the given E_γ and θ_{π^0} bins. N_s is the number of scalers in the given E_γ bin. ϵ_{tagg} is the tagging efficiency in the given E_γ bin and ϵ_{det} is the detection efficiency in the given E_γ and θ_{π^0} bins. ρ_a is the target surface density in *nuclei/cm²*. $\Gamma_{\gamma\gamma}$ is the branching ratio of the decay, and Ω is the solid angle of detection, defined as:

$$\Omega = \int_{\phi_1}^{\phi_2} d\phi \int_{\theta_1}^{\theta_2} \sin\theta d\theta \quad (5.9)$$

5.6 Error Analysis

The cross section calculations are laden with the systematical and statistical uncertainties.

Systematic errors are uncertainties in the bias of the data [53]. A simplest

example would be an offset of the measuring instrument, contrary to the random errors where each measurement fluctuates independently of the others, in case of systematical uncertainty, the entire data set is affected in exactly the same way.

In this experiment, one of the sources of the systematic error is the uncertainty due to the surface density calculations. It arises from the target thickness measurements, and for the ^{116}Sn and ^{124}Sn targets, it is of order $\sim 1\%$ and for the ^{120}Sn target it is $\sim 2\%$.

Another source of systematic error is from the fitting procedure for the π^0 missing energy spectrum.

There were three sources of the statistical error: the error on the tagging efficiency measurement, the error on the number of π^0 's in each E_γ and θ_π bins and the error on the number of the generated events for the π^0 detection efficiency calculations.

In general, statistical errors arise from the stochastic fluctuations, and in nuclear and particle physics they come from the observation of the Poisson distributed data. In such case, the error decreases with the increasing number of measurements.

The error on the the number of π^0 's in each E_γ and θ_π bins have been obtained from the analysis of the π^0 missing energy spectra, where in the coherent peak the error was of order $\sim 1\%$. The statistical error here comes from the number of the detected π^0 's and statistical uncertainty associated with the tagger random subtraction.

The uncertainty in the number of the generated events for the detection efficiency calculations have been chosen so the error on detection efficiency is no greater than the error on the number of π^0 's in each E_γ and θ_π bins, i.e. $\sim 1\%$.

The systematic error on the tagging efficiency measurement is of order of $\sim 1\%$ for all the channels and all the targets.

Chapter 6

Results

This chapter presents the results of the measurements of the cross sections of the coherent π^0 photoproduction on ^{116}Sn , ^{120}Sn and ^{124}Sn . The experimental data are compared with the theoretical DREN Kamalov's calculations.

6.1 Cross sections

The three tin isotopes have been chosen for this experiment because they are all stable nuclei and because their proton number is a magic number. Also, investigating the nuclear matter structure along the isotopic chain offers an additional advantage that the data for each target can be compared with each other without a systematic error due to charge distribution, and therefore allows to accurately measure the changes in the nuclear structure predicted by different models. The details of the targets used in the study are summarized in the table 3.3, in chapter 3.

The differential cross sections for all the targets are presented in figures 6.1 - 6.3. The diffraction pattern due to the form factor presence in the cross section is clearly visible.

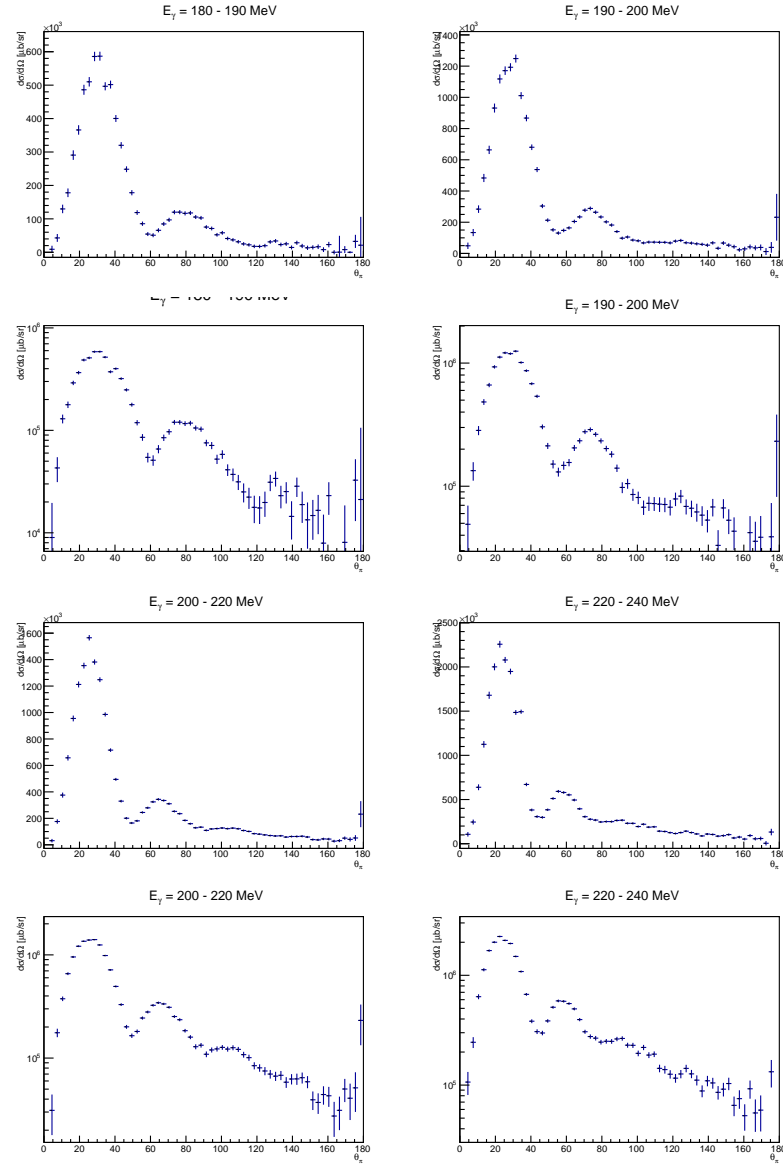


Figure 6.1: Differential cross sections for the ^{116}Sn target for a sample of photon energy bins in the E_γ range of $180 - 240\text{MeV}$.

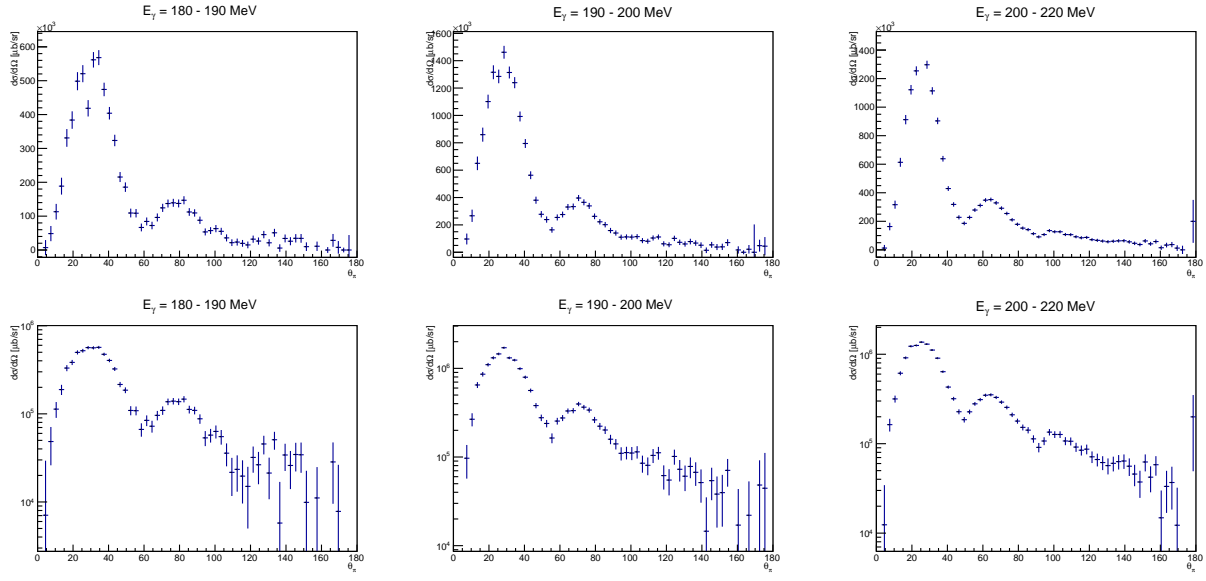


Figure 6.2: Differential cross sections for the ^{120}Sn target for a sample of photon energy bins in the E_γ range of $180 - 240\text{MeV}$.

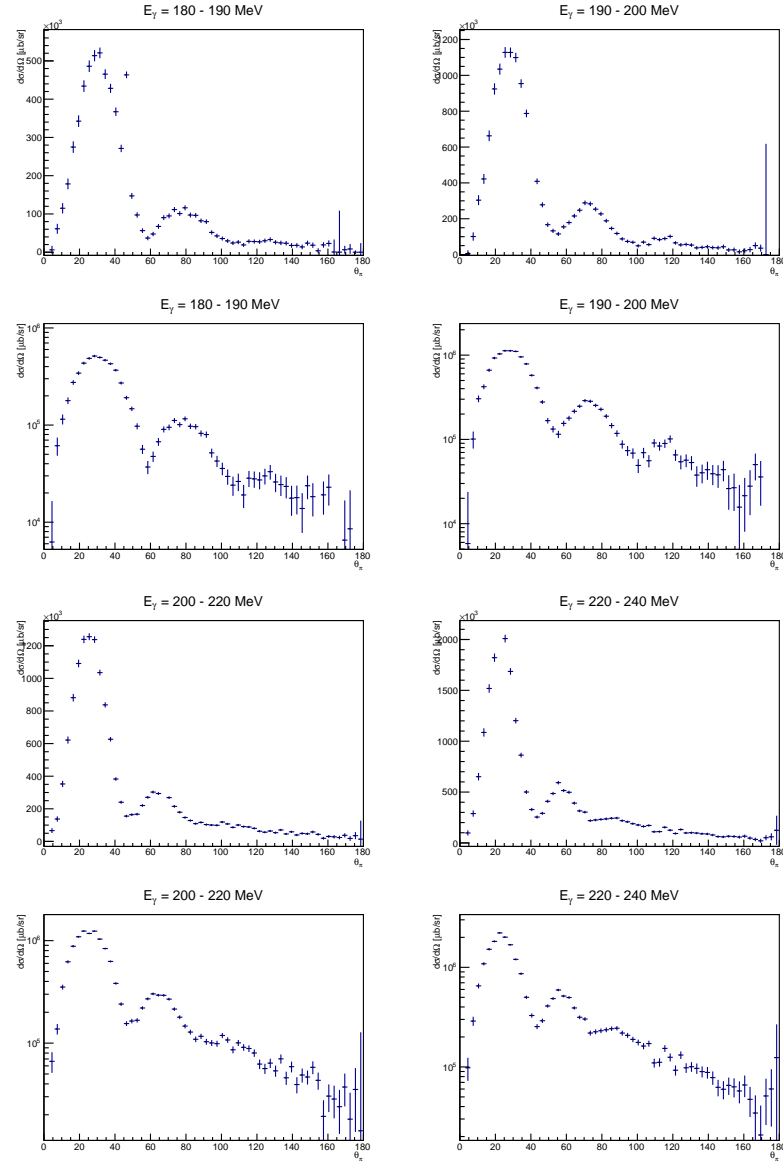


Figure 6.3: Differential cross sections for the ^{124}Sn target for a sample of photon energy bins in the E_γ range of $180 - 240\text{MeV}$.

The calculations of the ratio of cross sections have been performed in order to investigate the changes in the nuclear structure of the isotopes without the systematic error bias. Figures 6.4 to ?? present the ratios of the targets cross sections compared with the theoretical predictions from the Kamalov's DREN calculations.

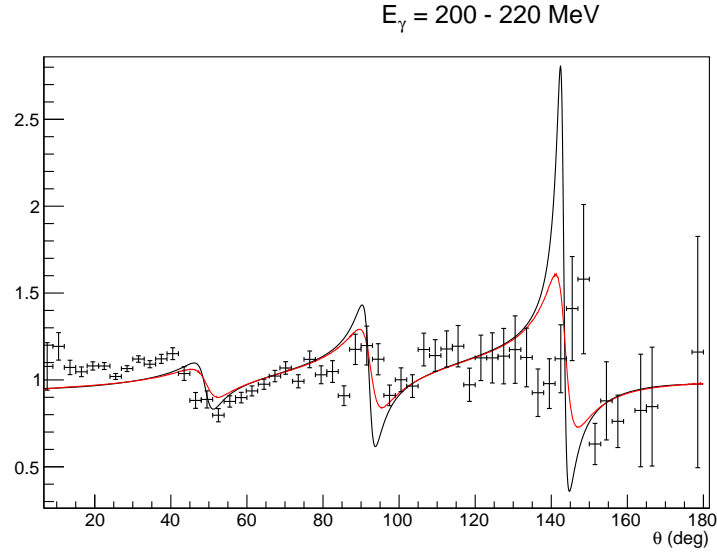


Figure 6.4: The ratio of the cross sections of ^{116}Sn to ^{120}Sn for the E_γ bin 200MeV . The black line is the Kamalov's DREN calculations and the red line is those calculations smeared with the energy resolution.

The dependence of the energy resolution on θ for different targets and photon energies is shown in the figures below. Those data have been fitted with a third degree polynomial function which was then used in the DREN calculations to reflect the effect of the energy resolution on the ratio of the cross sections predictions.

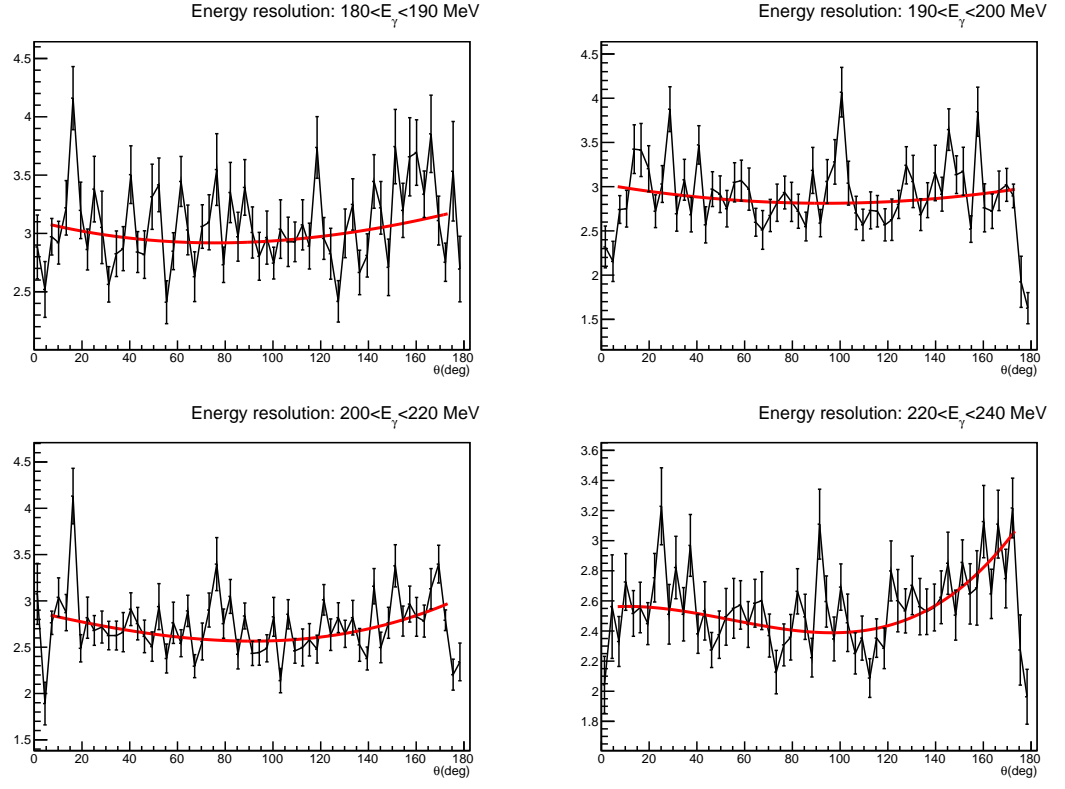


Figure 6.5: Plots of the energy resolution dependence on θ and E_γ for the ^{116}Sn target.

Bibliography

- [1] *CNS Data Analysis Center*, <http://gwdac.phys.gwu.edu>.
- [2] *The MAID Homepage*, <http://www.kph.uni-mainz.de/MAID>.
- [3] Proposal for an experiment: neutron skin evolution in isotopes of tin and calcium from coherent pion photoproduction, 2009.
- [4] *A2 MAMI website*, <http://wwwa2.kph.uni-mainz.de>. 2015.
- [5] S. Abrahamyan and et al. Measurement of the neutron radius of ^{208}Pb through parity violation in electron scattering. *Phys. Rev. Lett.* *108*, page 112502, 2012.
- [6] J. Albert. *Test Measurements for the Crystal Ball Detector at MAMI*, *PhD thesis*. 2003.
- [7] G.D. Alkhazov, S. L. Belostotsky, and A. A. Vorobyov. *Phys. Rep.* *42*, page 89, 1978.
- [8] C. Amsler and et al. *Phys. Lett. B* *667*, page 1, 2008.
- [9] J. R. M. Annand. *Data Analysis within an AcqRoot Framework*. *nuclear.gla.ac.uk/acqusys/doc/AcquRoot.11.08.pdf*. 2008.
- [10] S. Schamand B. Krusche. *Prog. Part. Nucl. Phys.* *51*, 399, 2003.
- [11] C. J. Batty and et al. *Adv. Nucl. Phys.* *19*, page 1, 1989.
- [12] C. Bertulani. *Nuclear Physics in a Nutshell*. Princeton University Press, 2007.
- [13] J. Bjorken and S. Drell. *Relativistic Quantum Mechanics*. McGraw Hill, New York, 1964.
- [14] B. A. Brown. Neutron radii in nuclei and the neutron equation of state. *Phys. Rev. Lett* *85* 25, 2000.
- [15] R. Brun. *Root manual*, root.cern.ch.
- [16] J. Carlson and R. Schiavilla. Quantum monte carlo calculations of $A = 9, 10$ nuclei. *Rev. Mod. Phys.* *70-3*, page 743, 1998.
- [17] R. Davidson. *Czechoslovak Journal of Physics* *44*, 365, 1994.

-
- [18] H. de Vries and et al. *At. Nuc. Dat. Nuc. Dat. Tab.* 36, page 495, 1987.
- [19] M. Dehn and et al. *Eur. Phys. J. Special Topics* 198, page 1947, 2011.
- [20] D. Drechsel. *European Physical Journal A* 34, 69, 2007.
- [21] J. Dudek. *Meson and baryon spectroscopy from Lattice QCD*.
<http://irfu.cea.fr/Documentation/Conferences/webCALS12/Talks/March9/dudek.pdf>, 2011.
- [22] A. Starostin et al. *Phys.Rev.C* 64, pages 55–205, 2001.
- [23] A. V. Dobrovolsky et al. *NPA*, page 766, 2006.
- [24] Audit et al. *Nuc. Inst. Meth. A* 301, pages 473–481, 1991.
- [25] C. J. Horowitz et. al. *Phys. Rev. C* 63, page 025501, 2001.
- [26] C. Tarbert et. al. *Phys. Rev. Lett.* 112, page 242502, 2014.
- [27] D. Drechsel et. al. *Nuc. Phys. A* 660, pages 423–438, 1999.
- [28] D. Vautherin et. al. *Phys. Rev. C* 5, page 626, 1972.
- [29] F. J. Fattoyev et al. Pure neutron matter constraints on the relativistic mean-field and skyrme-hartree-fock models. *arXiv:1205.0857v1*, 2012.
- [30] G. Bruan et al. Tdc chip and readout driver developments for compass and lhcx experiments. *arXiv:hep-ex*, 1998.
- [31] G. J. Igo et. al. *Rev. Mod. Phys.* 50, page 523, 1978.
- [32] G.D. Alkhazov et. al. *Phys.Atom.Nucl.* 78, pages 381–386, 2015.
- [33] J. Beringer et al. *The Review of Particle Physics*, *Phys. Rev. D* 86, 2012.
- [34] J. Decharge et. al. *Phys. Rev. C* 21, page 1568, 1980.
- [35] K. Pomorski et. al. *Nuc. Phys. A* 624, pages 349–369, 1997.
- [36] Lie-Wen Chen et al. *Phys. Rev. C* 72. 2005.
- [37] Lie-Wen Chen et al. *Proceedings of the 13th National Conference on Nuclear Structure in China*. 2011.
- [38] M. Centelles et al. *Phys Rev Lett.* 102, pages 122–502, 2009.
- [39] M. Oreglia et al. *Phys. Rev. D.* 25, page 9, 1982.
- [40] P. Danielewicz et al. *Nucl. Phys. A* 727, page 233, 2003.
- [41] R. Arndt et al. *Physical Review C* 42, 1853, 1990.
- [42] S. Pieper et. al. Quantum monte carlo calculations of $a = 9, 10$ nuclei. *Phys. Rev. C* 66, page 044310, 2002.

- [43] S. R. Neumaier et al. *Nucl.Phys. A* 712, page 247, 2002.
- [44] T. Takaki et. al. *Nucl. Phys. A* 443, pages 570–588, 1985.
- [45] G. Fricke and et al. *At. Nuc. Dat. Nuc. Dat. Tab.* 60, pages 177–285, 1995.
- [46] F. E. Low G. F. Chew, M. L. Goldberger and Y. Nambu. *Phys. Rev.*, 106:1345-1355, 1957.
- [47] T. Gesslerr. *Bachelor thesis*. Universitaet, Giessen, 2008.
- [48] S.J. Hall, G.J. Miller, R. Beck, and P. Jennewein. *Nucl. Instrum. Methods A* 368, page 698, 1996.
- [49] K.Iida and K. Oyamatsu. *Phys. Rev. C* 69, page 037301, 2004.
- [50] G.F. Knoll. *Radiation Detection and Measurement*. John Wiley and Sons.
- [51] D. Krambrich. *University of Mainz, PhD thesis*.
- [52] B. Lemmer. *Diploma thesis*. Universitaet, Giessen, 2007.
- [53] W. R. Leo. *Techniques for Nuclear and Particle Physics Experiments*. Springer-Verlag, 1992.
- [54] B. Martin and G. Shaw. *Particle Physics*. Wiley and sons, 2008.
- [55] J. McAndrew. *PhD thesis*. University of Edinburgh, 2011.
- [56] J C. McGeorge and J. D. Kellie et al. *Eur. Phys. J. A*, 37, pages 129–137, 2008.
- [57] A. Meucci. *Relativistic Mean Field Theory of Nuclear Structure, Pavia*. 2000.
- [58] D. Middleton. *Mainz a2 tagger calibrations a2 internal report.*, 2011.
- [59] G.J. Miller and R. O. Owens. *Nuc. Ins. and Meth.*, pages 390 257–266, 1997.
- [60] V. D. A. Nagl and H. Uberall. *Nuclear Pion Photoproduction*. Springer-Verlag, 1991.
- [61] R. Novotny. *IEEE Trans. Nucl. Sci.* 38, page 2, 1991.
- [62] J. Piekarewicz. *Phys. Rev. C* 73, page 044325, 2006.
- [63] J. Piekarewicz. *Phys. Rev. C* 76, page 031301, 2007.
- [64] J. Piekarewicz. *Phys. Rev. C* 76, page 064310, 2007.
- [65] J. Piekarewicz. Private communication, 2015.
- [66] J. Piekarewicz and S. Pieper. *Nucl. Phys. A* 778, page 10, 2006.
- [67] P. Ring and P. Schuck. *The Nuclear Many-Body Problem*. Springer Verlag, Heidelberg, 1980.

- [68] X. Roca-Maza, M. Centelles, X. Vinas, and M. Warda. *Phys. Rev. Lett.* *106*, page 252501, 2011.
- [69] M. E. Roebig. *Diploma thesis*. Universitaet Giessen, 1991.
- [70] L. Schmitt. *IEEE Trans.Nucl.Sci.*, pages 51:438–444, 2004.
- [71] Zongqiang Sheng and Zhongzhou Ren. *Eur. Phys. J. A* *46*, pages 241–247, 2010.
- [72] I. Sick and J. S. MacCarthy. *Nucl. Phys. A* *150*, page 631, 1980.
- [73] C. M. Tarbet. *Coherent π^0 photoproduction on nuclei*. University of Edinburgh, 2007.
- [74] A. Trzcinska. Antiprotonic atoms as a tool to study the nuclear periphery. *A. Phys. Pol. B.* *41*, 2010.
- [75] M. Unverzagt. *Diploma thesis*. University of Mainz, 2004.
- [76] M. Unverzagt. *Nucl.Phys.Proc.Suppl.* *198*, pages 174–181, 2010.
- [77] R. Walker. *Phys. Rev.* *182*, 1729, 1969.